

ScholarWorks@GSU

Ultrafast Electron Dynamics in Transition Metal Dichalcogenide Materials

Authors	Hossaini, Sayed Jaber
Citation	Hossaini, Sayed Jaber. "Ultrafast Electron Dynamics in Transition Metal Dichalcogenide Materials." 2024. Dissertation, Georgia State University. https://doi.org/10.57709/38091670
DOI	https://doi.org/10.57709/38091670
Download date	2026-04-15 23:50:31
Link to Item	https://hdl.handle.net/20.500.14694/12324

Ultrafast Electron Dynamics in Transition Metal Dichalcogenide Materials

by

Sayed Jaber Hossaini

Under the Direction of Vadym Apalkov, Ph.D.

A Dissertation Submitted in Partial Fulfillment of the Requirements for the Degree of

Doctor of Philosophy

in the College of Arts and Sciences

Georgia State University

2024

ABSTRACT

In this dissertation, we theoretically explore the ultrafast nonlinear process in nanoflakes of 2D materials placed in the field of a femtosecond-long optical pulse. The duration of a pulse is of the order of a few femtoseconds and its amplitude is in the range of 0.1-1.5 V/Å. To be more specific, we study ultrafast electron dynamics in transitional metal dichalcogenides (TMDCs) quantum dots. Different sizes of quantum dots (QD) of a hexagonal shape are considered. Taking into account that the valence and conduction bands of TMDC materials are mainly formed by d orbitals of the corresponding metal atoms, we consider a three-band tight binding model of TMDC, where the spin-orbit coupling is also included into the model. The energy spectra were calculated for different sizes of TMDC QDs and, for all cases, the anticipated in-gap edge states were observed. With increasing the QD size, the band gap decreases and asymptotically approaches the band gap of the corresponding TMDCs monolayer. In the thesis, two nonlinear characteristics of electron dynamics in TMDC QDs are considered. The first one is the absorption of an optical pulse by TMDC QDs. Such an absorption is determined by the residual electron population of the excited QD states, i.e., population after the pulse. As a function of the field amplitude, the absorption first increases at low amplitudes, shows a peak at an intermediate amplitude, and then converges to a constant value at high amplitudes. The second characteristic of nonlinear electron dynamics is the high harmonic generation, which is determined by the time dependence of the generated electron dipole moment during the pulse. The generation of high optical harmonics was studied for different TMDC materials, different QD sizes, and different characteristics of the optical pulse. One of the characteristics of the corresponding radiation spectrum is the cutoff frequency, which is the highest-order harmonics that can be generated for the pulse of a given intensity. As a function of the QD size, the cutoff frequency shows the maximum value at intermediate QD sizes, which is realized for TMDC QD consisting of around 61

metal atoms. Such nonmonotonic dependence of the radiation spectra on the parameters of TMDC QD shows that the strongest nonlinear optical response of TMDC QDs occurs at QD of a finite size.

INDEX WORDS: 2D Material, transitional metal dichalcogenides, d orbitals, quantum dots, tight binding model, Hamiltonian, spin-orbit coupling, band gap, in-gap edge states, dipole moment, high harmonic generation, cutoff frequency.

Copyright by
Sayed Jaber Hossaini
2024

Ultrafast Electron Dynamics in Transition Metal Dichalcogenide Materials

by

Sayed Jaber Hossaini

Committee Chair:

Vadym Apalkov

Committee:

Unil Perera

Steve Manson

Electronic Version Approved:

Office of Graduate Services

College of Arts and Sciences

Georgia State University

December 2024

DEDICATION

To my loving family.

ACKNOWLEDGMENTS

”In the name of God, the Most Gracious, the Most Merciful” I would like to express my most profound appreciation to Professor Vadym Apalkov and Professor Mark I. Stockman for their guidance and advice during my PhD program. I believe that I am tremendously fortunate to have them as my advisors. My sincerest gratitude and thanks also go to my committee members: Dr. Steven Mason and Dr. Unil Perera for supporting the scientific ideas in my dissertation. I am extending my thanks to the graduate adviser, Dr. Murad Sarsur, the chair of physics and astronomy department, Dr. Sumith Doluweera, Dr. Brian Thomes and all other professors at GSU for enriching classes. I am extremely grateful to my parents and brothers for their continuous love, prayers, support, and encouragement. I am so lucky to have a great family.

TABLE OF CONTENTS

ACKNOWLEDGMENTS		v
List of Tables		vii
LIST OF FIGURES		viii
1 Introduction:		1
1.1 Interaction of matter and pulse:		1
1.2 2D materials		5
1.3 Electronic properties:		7
1.4 Valleytronics:		9
2 Methods and equations:		12
3 Absorption in Transitional Metal Dichalcogenides		17
3.1 Introduction:		17
3.2 Method:		18
3.3 Results and Discussion:		19
3.4 Conclusion:		33
4 High Harmonic Generation:		35
4.1 Introduction:		35
4.2 Method:		36
4.3 Results and Discussion:		38
4.4 Conclusion:		51
5 Summary:		52
REFERENCES		54

List of Tables

LIST OF FIGURES

Figure 1.1 The crystal structure of TMDCs monolayer showing a layer of transition metal atoms (blue) sandwiched between two layers of dichalcogenide atoms (yellow).	6
Figure 1.2 (color online) Orbital projected band structures for monolayer MoS_2 from FP calculations. (a) contribution from Mo d orbitals: blue dots for d_{xy} and $d_{x^2-y^2}$, red open circles for d_{z^2} , and green open diamonds for d_{xz} and d_{yz} . (b) Total p orbitals, which are dominated by S atoms. (c) Total S orbitals.	7
Figure 1.3 Band structure diagram of (left) bulk and (right) monolayer MoS_2 showing the crossover from indirect to direct bandgap accompanied by a widening of the bandgap[22].	8
Figure 1.4 a) σ^+ = circularly polarized light incident on a MoS_2 monolayer excites charge carriers in the K- valley (orange spheres). Light with the frequency equal to the A-exciton binding energy (red arrow) excites spin-up electrons and spin-down holes. Conversely, light corresponding to the B-exciton (blue arrow) excites spin-down electrons and spin-up holes. An in-plane electric field causes electrons to accumulate on one edge of the layer, and holes on the other one. b) σ^- light excites charge carriers in the K'-valley (green) with the spins opposite to those in the K-valley, with the charges also accumulating on the opposite edges. c) Linearly polarized light with the energy equal to the binding energy of the A-exciton excites charges in both valleys, with carriers carrying the same spins collecting on the same layer edge.	11
Figure 3.1 Hexagonal MoS_2 quantum dot. It consists of Mo (filled red dots) and S (open dots) atoms. The quantum dot shown in the figure has the size of $N_e = 19$. The dashed line illustrates the hexagonal shape of the quantum dot.	19
Figure 3.2 Energy spectra of MoS_2 QD of sizes $N_e = 19, 61, 91$. The inset shows the size of the band gap vs N_e . As QD size increase the band gap decreases.	21
Figure 3.3 Energy spectra of MoS_2 QD of sizes $N_{Mo} = 19, 61, 91$. The inset shows the size of the band gap vs N_{Mo} . As QD size increase the band gap decreases.	22
Figure 3.4 shows the electric field of an optical pulse vs time(femtosecond) for one oscillation.	23

Figure 3.5	Absorbance as a function of the pulse amplitude. The duration of the pulse is $\tau = 2fs$. The results are shown for three different wavelengths: $\lambda = 400nm, 600nm,$ and $820nm$. The size of MoS_2 QD is $N_{Mo} = 19$	25
Figure 3.6	Absorbance as function of wavelength of the optical pulse. The amplitude of the pulse is $F_0 = 0.5V/\text{\AA}$ and its duration is $\tau = 2fs$. The sizes of MoS_2 QD are $N_{Mo} = 19$	26
Figure 3.7	Absorbance as a function of the field amplitude, F_0 . The wavelength of the pulse is 820 nm. The absorbance is shown for the three duration of the pulse: $\tau = 2fs, 3fs,$ and $4fs$. The size of MoS_2 QD is (a) $N_{Mo} = 19,$ (b) $N_{Mo} = 61,$ and (c) $N_{Mo} = 91$	28
Figure 3.8	Residual population, i.e., population after the pulse, of the QD levels. The wavelength of the pulse is 820 nm and its duration is $\tau = 2fs$. The pulse amplitude is (a) and (d) $F_0 = 0.1V/\text{\AA};$ (b) and (f) $F_0 = 0.5V/\text{\AA};$ (c) and (g) $F_0 = 1.5V/\text{\AA}$. The size of the QD is (a), (b), (c) $N_{Mo} = 19;$ (d), (f), (g) $N_{Mo} = 61$	30
Figure 3.9	absorbance as function of the field amplitude, F_0 . The wavelength of the pulse is 820 nm and the durations of the pulse is $\tau = 2fs$. The size of the QD is $N_{Mo} = 61$. The TMDC materials are labeled next to the corresponding lines. The inset shows the bulk bandgaps of the corresponding materials. . .	32
Figure 4.1	(a) electric field of the incident pulse as the function of time. The pulse is linearly polarized in the x-direction. (b) The generated dipole moment of a TMDC QD. Here both the x and y components of the dipole moment are generated. The electron dynamics in the field of the pulse is nonreversible, which is visible as a non-zero residual dipole moment.	38
Figure 4.2	Radiation spectra of a TMDC QD as a function of frequency. The pulse is linearly polarized along the x-direction. The amplitude of the pulse is shown next to each line.	39
Figure 4.3	Radiation spectra of MoS_2 QD in the field of a linearly polarized pulse. The pulse is polarized along the x -direction. The duration of the pulse and size of a QD, i.e., the number of Mo atoms in QD are the following: (a)-(c) $N_{Mo} = 19$ and the duration of the pulse is $\tau = 2$ fs (a) 3 fs (b), and 4 fs (c); (d)-(f) $N_{Mo} = 61$ and the duration of the pulse is for $\tau = 2$ fs (d) 3 fs (e) and 4 fs (f); (g)-(I) $N_{Mo} = 91$ and the duratino of the pulse is $\tau = 2$ fs (g) 3 fs (h), and 4 fs (I). The amplitude of the pulse is marked in each panel. The frequency of the pulse is 2.3 rad/fs.	41

Figure 4.4	The intensities of high-order harmonics (the 6th, 8th, and 10th harmonics) as a function of the field amplitude. The pulse is linearly polarized in the x -direction. The hexagonal MoS ₂ QD consists of 61 Mo atoms. The duration of the pulse is 2 fs and its frequency is 2.3 rad/fs.	42
Figure 4.5	Cutoff frequency as a function of the field amplitude. The QD size, i.e., the number of Mo atoms, is $N_{Mo} = 19$ (a), 61 (b), and 91 (c). The duration of the pulse is marked at each panel. The frequency of the pulse is 2.3 rad/fs.	44
Figure 4.6	Cutoff frequency versus the field amplitude for different values of the frequency of the pulse, ω . The QD size is 19, i.e., the QD consists of 19 Mo atoms. The pulse duration is 2 fs.	46
Figure 4.7	Cutoff frequency versus a QD size. The amplitude of the pulse is $F_0 = 0.5V/A$, its frequency is $\omega = 2.3$ rad/fs, and its duration is $\tau = 2$ fs. . .	48
Figure 4.8	Intensity of the 5 th harmonic versus the pulse field amplitude for different QD sizes. Here $\omega = 2.3$ rad/fs and $\tau = 3$ fs. The QD sizes, which are characterized in terms of the number of Mo atoms, are m	50

CHAPTER 1

Introduction:

Modern light generation technology offers extraordinary capabilities for sculpting light pulses, with full control over individual electric field oscillations within each laser cycle (1; 2; 3). Progress in laser technology made it possible to generate ultrashort pulses with fields comparable to the internal fields in solids and with the duration of just a few femtoseconds ($1\text{fs} = 10^{-15}$) (4; 5; 6; 7; 8; 9). Interaction of light and matter at femtosecond time scale is approximately an adiabatic process because transmitted energy as heat is minimal, allowing one to study and explore field-driven electron dynamics with higher precision. In the following, we start with basic physics of light-matter interactions (10).

1.1 Interaction of matter and pulse:

Classically, light-matter interaction is the interaction of an oscillating electromagnetic field with charged particles in the matter, most often bound electrons. This process is observed through changes to the light induced by the matter, such as absorption or emission of light, or by light-induced changes to the matter, such as ionization and photochemistry. By studying such processes as a function of the control variables for the light fields (amplitude, frequency, polarization, phase, ect) we can deduce the properties of the samples. Quantum mechanically we consider the interaction of light-matter as a perturbation induced by the electric and magnetic fields of the light that couple quantum states of the charged particle in matter.

To derive the Hamiltonian of a charged particle interacting with the field of a pulse in the term of vector potential we start with the Lorentz force on a particle with charge q :

$$F = q(E + v \times B). \quad (1.1)$$

Here E and B are electric and magnetic fields, respectively and v is the velocity of a charged particle. Rewriting the above expression for one direction, for example, the x -direction, in Cartesian coordinate system, we obtain the following expression

$$F_x = q(E_x + v_y B_z - v_z B_y) \quad (1.2)$$

In Lagrangian mechanics, this force can be expressed in terms of the total potential energy U as follows

$$F_x = -\frac{\partial U}{\partial x} + \frac{d}{dt} \frac{\partial U}{\partial v_x}. \quad (1.3)$$

Inserting equation 1.2 into equation 1.3 we get the following identity

$$U = q\varphi - q\vec{v} \cdot \vec{A}. \quad (1.4)$$

Here φ is the corresponding electric potential and \vec{A} is the corresponding magnetic field vector potential.

On the other hand, the Lagrangian is expressed in the terms of the kinetic and potential energy of the particle, i.e.,

$$L = T - U, \quad (1.5)$$

$$L = \frac{1}{2}m\vec{v}^2 + q\vec{v} \cdot \vec{A} - q\varphi$$

Then the Hamiltonian of the particle becomes

$$H = \vec{p} \cdot \vec{v} - L = \vec{p} \cdot \vec{v} - \frac{1}{2} m \vec{v}^2 - q \vec{v} \cdot \vec{A} - q\varphi. \quad (1.6)$$

Taking into account that

$$p = \frac{\partial U}{\partial \vec{v}} = m\vec{v} + q\vec{A}, \quad (1.7)$$

We obtain

$$H = \frac{1}{m} \vec{p} \cdot (\vec{p} - q\vec{A}) - \frac{1}{2m} (\vec{p} - q\vec{A})^2 - \frac{q}{m} (\vec{p} - q\vec{A}) \cdot \vec{A} + q\varphi,$$

or

$$H = \frac{1}{2m} [\vec{p} - q\vec{A}(\vec{r}, t)]^2 + q\varphi(\vec{r}, t). \quad (1.8)$$

This expression is the classical Hamiltonian for a particle in the field of the pulse. For a collection of charged particles the Hamiltonian can be expressed as follows

$$H = \sum_i \left(\frac{1}{2m_i} (\vec{p}_i - q_i \vec{A}(\vec{r}_i))^2 + V_o(\vec{r}_i) \right),$$

$$H = H_o - \sum_i \left(\frac{q_i}{2m_i} (\vec{p}_i \cdot \vec{A} + \vec{A} \cdot \vec{p}_i) + \sum_i \frac{q_i}{2m_i} |\vec{A}|^2 \right). \quad (1.9)$$

In quantum description, the Hamiltonian of a matter interacting with the light can be written in the following form: $H = H_M + H_L + H_{ML}$. A quantum treatment of the light would describe the light in terms of quantized states, i.e., photons corresponding to different modes of electromagnetic radiation. For a many-body system, time-dependent functional theory (DFT) is considered, where the field-driven electron dynamics is quantum mechanically described by the time dependent Kohn-Sham equations in the velocity gauge (11):

$$i\hbar \frac{\partial \Psi_i(\vec{r}, t)}{\partial t} = \left[\frac{1}{2m} (\vec{p} + \frac{e}{c} \vec{A}_{tot})^2 + V_{ion}(\vec{r}) + \int \frac{e^2}{|\vec{r} - \vec{r}'|} n(\vec{r}', t) + V_{xc}(\vec{r}, t) \right] \Psi_i(\vec{r}, t), \quad (1.10)$$

Where $n(\vec{r}, t) = \sum_i |\Psi_i(\vec{r}, t)|^2$ is the density, and $V_{xc}(r, t)$ is the exchange-correlation potential. The total vector potential A_{tot} is given by $A_{tot} = A_{ext} + A_{ind}$ where A_{ext} is the vector potential of the applied field, and A_{ind} is the induced vector potential due to induced polarization of a solid. In the time-dependent Kohn-Sham equations, the pulse-matter interaction can be also introduced in the length gauge within the dipole approximation(12), i.e.,

$$i\hbar \frac{\partial \Psi_i(\vec{r}, t)}{\partial t} = \left[-\frac{1}{2} \frac{\partial^2}{\partial^2 \mathbf{r}} + V_{ion} + \int \frac{e^2}{|\vec{r} - \vec{r}'|} n(\vec{r}', t) + V_{xc}(\vec{r}, t) + \vec{F}(t) \cdot \vec{r} \right] \Psi_i(\vec{r}, t), \quad (1.11)$$

Where $F(t)$ is the field of the laser pulse. This approach has been applied to a crystalline silicon subjected to a strong laser pulse with the intensity of $10^{10} - 10^{15} W/cm^2$ and the duration around $21 fs$ (13). However, DFT requires large simulation and long processing time which is not economically good approach(14).

In semiclassical approach, the rate equation is used to describe the noncoherent electron dynamics (15). In this approach, the carrier relaxation and generation times are taken into account. Also, the electric field of the pulse generates an electron-hole plasma through

multiphoton and electron avalanche ionizations. In this model, the ionization processes are included in the rate equation as follows

$$\frac{\partial n_e}{\partial t} = \frac{n_v - n_e}{n_v} (\omega_{PI} + n_e \omega_{II}) - \frac{n_e}{\tau_r}, \quad (1.12)$$

where n_e is the electron density, n_v is the initial electron density in the valence bands, ω_{PI} is photoionization rate in the units of $cm^{-3}s^{-1}$, ω_{II} is avalanche ionization rate in s^{-1} , and τ_r is the time constant.

1.2 2D materials

Two dimensional (2D) materials or single-layer materials refer to crystalline solids consisting of a single layer of atoms(16). The single-layer materials could be derived from a single element like graphene or compounds of two or more elements. Graphene is the first such 2D material that was discovered in 2004. Graphene can be mechanically exfoliated from bulk graphite and opened the door to investigation of a large variety of other 2D materials(17; 18). Among them, transition metal dichalcogenides (TMDCs) represent a class of promising materials that are the candidates for overcoming some of the disadvantages of graphene for future applications, such as ultrathin, flexible photonic and optoelectronic devices that require optically transparent semiconductors(19). Figure 1.1 illustrates a TMDC monolayer, which has a hexagonal layer of metal atoms (M) sandwiched between two hexagonal layers of chalcogen atoms (X). These monolayers can bond with each other and form a multilayer TMDCs(20).

TMDC monolayers can be regarded as a semiconductor analog of graphene. They have

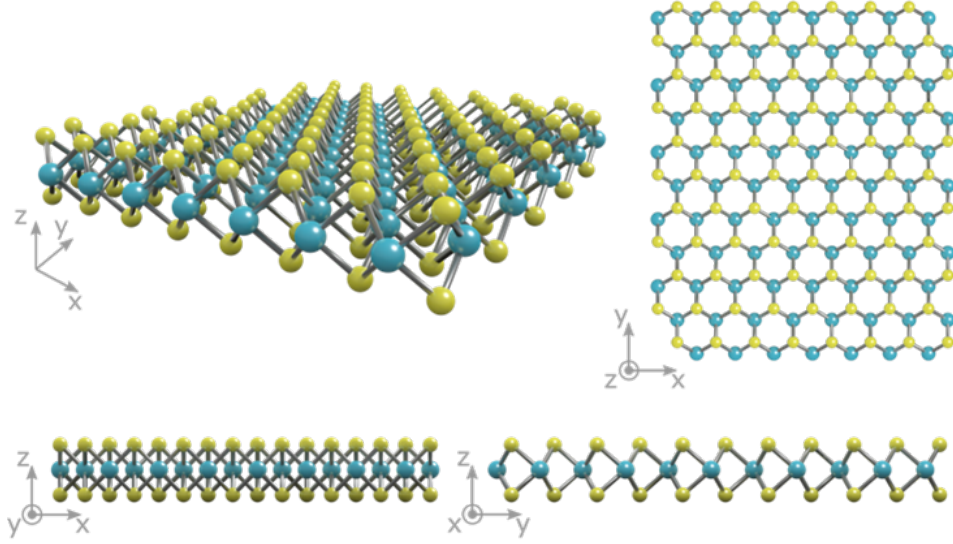


Figure 1.1 The crystal structure of TMDCs monolayer showing a layer of transition metal atoms (blue) sandwiched between two layers of dichalcogenide atoms (yellow).

honeycomb crystal structure but they are not centrosymmetric, because the M and X are different types of atoms, consequently inversion symmetry is broken. Due to broken inversion symmetry, the Berry curvature, is not singular as in graphene and has finite values with opposite signs at two valleys, K and K' . Another difference between TMDC materials and graphene is a strong intrinsic spin-orbit interaction in TMDC monolayers(21).

One of the TMDC materials is MoS_2 . The Bloch states of MoS_2 monolayer near the band edges mostly consist of Mo d orbitals, d_{z^2} , d_{xy} , and $d_{x^2-y^2}$. Figure 1.2 clearly shows that the contributions from the s orbitals are negligible, and those from the p orbitals are very small near the band edges. Thus, d_{z^2} , d_{xy} , and $d_{x^2-y^2}$ orbitals are dominant components for the conduction and valence bands. The trigonal prismatic coordination (Fig 1.2 (b)) splits the Mo d orbitals into three categories: $A'_1 = d_{z^2}$, $E' = d_{xy} + d_{x^2-y^2}$, and $E'' = d_{xz} + d_{yz}$, where A'_1 , E' and E'' are the Mulliken notations for irreducible representations (IRs) of point group

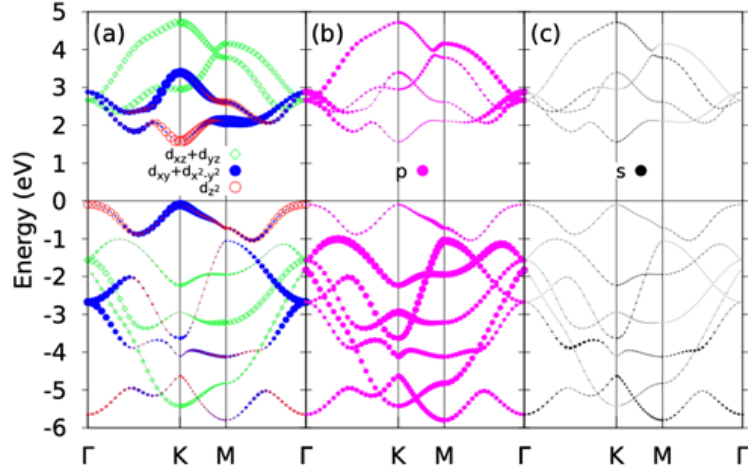


Figure 1.2 (color online) Orbital projected band structures for monolayer MoS_2 from FP calculations. (a) contribution from Mo d orbitals: blue dots for d_{xy} and $d_{x^2-y^2}$, red open circles for d_{z^2} , and green open diamonds for d_{xz} and d_{yz} . (b) Total p orbitals, which are dominated by S atoms. (c) Total S orbitals.

D_{3h} . The reflection symmetry in the xy plane allows hybridization of orbitals in A'_1 and E' categories only, leaving E'' decoupled from the A'_1 and E' states, see Figure 1.2 (a). The above analysis is also true for all MX_2 TMDCs monolayers. Therefore it is reasonable to construct a three-band tight binding model of a MX_2 monolayer by considering d-d hopping only by using the minimal set of $M - d_{z^2}$, d_{xy} , and $d_{x^2-y^2}$ orbitals as the basis(11).

1.3 Electronic properties:

Individual layers of MoS_2 have different properties compared to bulk. As figure 1.3 shows, if the interlayer interaction is removed, electrons confined to a single plane result in the formation of a direct bandgap and its size increases to 1.89 eV (22). The bandgap can be tuned by introducing strain into the structure. Experimental results showed a 300 meV

increase in the bandgap for each %1 biaxial compressive strain applied to trilayer MoS_2 . Photoluminescence spectra of MoS_2 monolayers show two excitonic peaks: one at $\sim 1.92eV$ (the A exciton), and the other one is at $\sim 2.08eV$ (the B exciton). These are attributed to the valence band splitting at the K-point (in the Brillouin zone), and allow two optically active transitions (23). The binding energy of the excitons is $> 500meV$, which shows that they are stable at high temperatures.

Injecting excess electrons into MoS_2 (by either electrical (24) or chemical (25) doping) can cause the formation of tritons (charged excitons), which consist of two electrons and one hole. They appear as peaks in the absorption and PL spectra that are red-shifted by $\sim 40 meV$ with respect to the A exciton peak. While the binding energy of tritons is much lower than that of the excitons (at approximately 20 meV), they have a non-negligible contribution to the optical properties of MoS_2 films at room temperature.

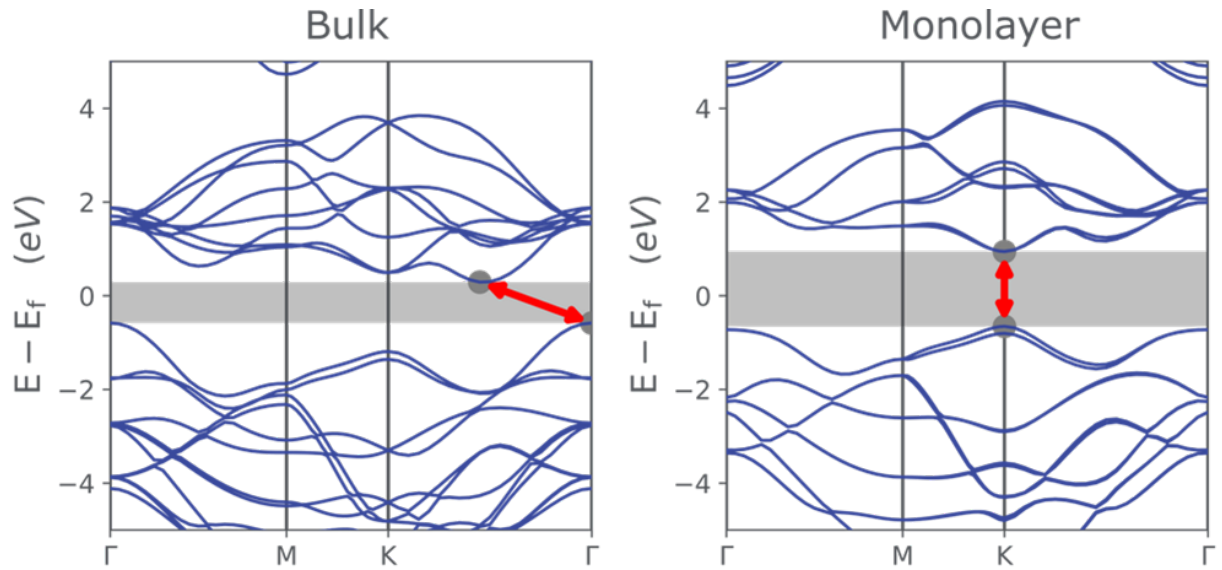


Figure 1.3 Band structure diagram of (left) bulk and (right) monolayer MoS_2 showing the crossover from indirect to direct bandgap accompanied by a widening of the bandgap[22].

1.4 Valleytronics:

MoS_2 monolayer and other 2D TMDCs may offer a route to technologies beyond electronics, where the valley degrees of freedom (other than charge) can be utilized for information storage and processing (26). The electronic band structure of MoS_2 monolayer displays the energy maxima in the valence band and the minima in the conduction band at both the K and K' (often called -K) points of the Brillouin zone. These two discrete 'valleys' have the same energy gap but are distant in the momentum space.

The optical transitions in these two valleys require angular momentum changes by +1 for the K-point, and -1 for the K' point (27). Hence, excitons can be excited in the corresponding valley with a circularly polarised light: excitons in the K valley can be excited with a right-handed (σ^+) polarized pulse, while excitons in the K' valley can be excited with a left-handed (σ^-) polarised light.

Conversely, light emitted due to exciton recombination in the K valley is σ^+ polarised, and light emitted due to exciton recombination in the K' valley is σ^- polarised. Since these valleys can be independently excited, they represent a degree of freedom called 'valley pseudospin' (28) that could be used in 'valleytronic' devices.

Furthermore, the spin-orbit interaction splits the energy states in the valence band at the K and K' points and carriers have opposite signs of spin for each of the valleys (29). For example, in K valley an A-exciton consists of a spin-up electron and a spin-down hole, and B-exciton has a spin-down electron and spin-up hole. For A and B excitons in the K' valley, their constituent charge carriers have the opposite spins. This property means that the valley

pseudospin and the charge carrier spin are coupled (spin-valley coupling). Therefore spin and valley properties of charge carriers can be selected optically(30).

When an in-plane electric field is applied, excitons may become disassociated (31), while the carriers retain their valley and spin characteristics. Electrons (and holes) in opposing valleys will travel in opposite directions perpendicular to the field. This is called the 'valley Hall effect', and could form the basis of future technologies, where more information can be encoded onto electrons because of the extra degree of freedom.

Excitons in MoS_2 monolayers have a valley lifetime (the time they remain in their original valley before scattering out) of a few picoseconds. In comparison, the valley lifetime of electrons is > 100 nanoseconds, and holes may have an even longer lifetime (32). The valley lifetime introduces limitations on the time available to complete logic operations using the valley pseudospin.

Charge carrier spins following selective optical excitation.

	σ^+ (K valley)	σ^- (K' valley)
E_A	$\uparrow e \downarrow h$	$\downarrow e \uparrow h$
E_B	$\downarrow e \uparrow h$	$\uparrow e \downarrow h$

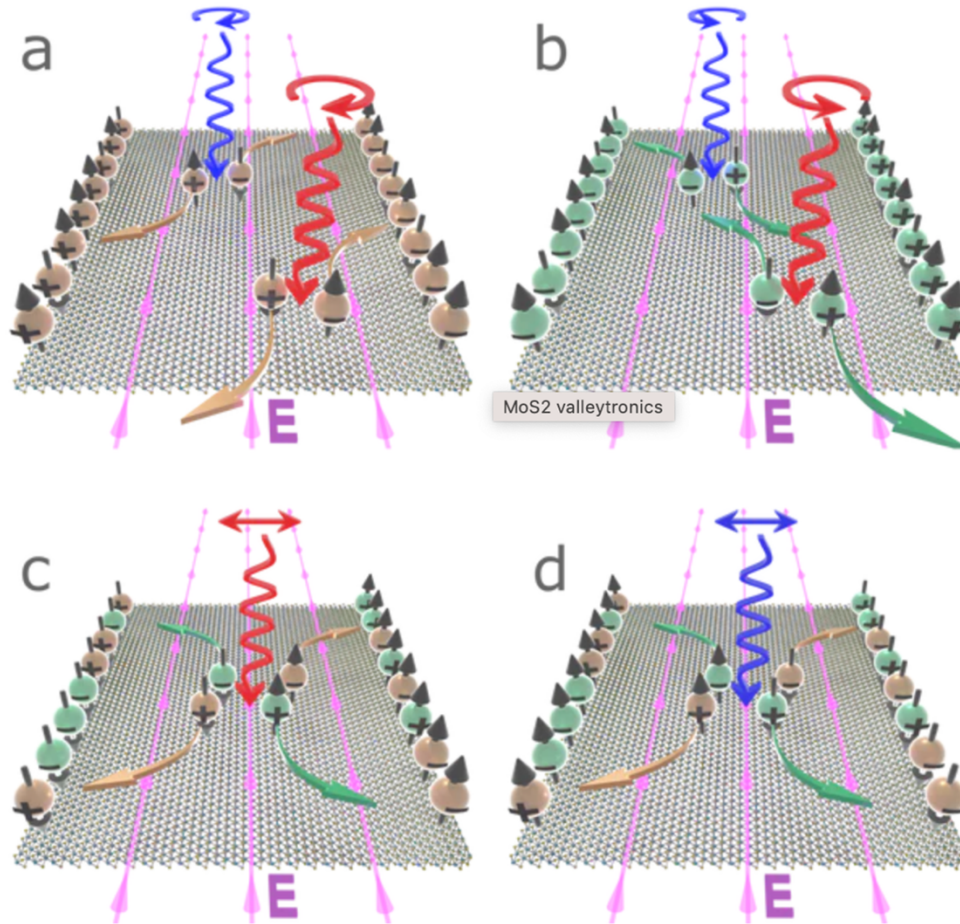


Figure 1.4 a) σ^+ = circularly polarized light incident on a MoS_2 monolayer excites charge carriers in the K- valley (orange spheres). Light with the frequency equal to the A-exciton binding energy (red arrow) excites spin-up electrons and spin-down holes. Conversely, light corresponding to the B-exciton (blue arrow) excites spin-down electrons and spin-up holes. An in-plane electric field causes electrons to accumulate on one edge of the layer, and holes on the other one. b) σ^- light excites charge carriers in the K'-valley (green) with the spins opposite to those in the K-valley, with the charges also accumulating on the opposite edges. c) Linearly polarized light with the energy equal to the binding energy of the A-exciton excites charges in both valleys, with carriers carrying the same spins collecting on the same layer edge.

CHAPTER 2

Methods and equations:

In this dissertation we study interaction of 2D materials with an ultrashort pulse. We start with the Hamiltonian of the 2D material, H_0 , which is derived by the tight-binding method for a transitional metal dichalcogenide (TMDCs) monolayer. The Hamiltonian also take into account that the transitional metal elements in these materials have a strong spin orbit coupling (SOC). A laser pulse with the amplitude around $0.1 - 1.5V/A$ and the duration of $2 - 4fs$ is applied to a nanoflake of such a material, i.e., quantum dot (QD) of TMDC monolayer. The complete dynamics is described by time dependent Schrodinger equation (TDSE) which has the following form

$$H(t) = H^{TNN} + H^{SOC} + eF(t).r$$

$$i\hbar\frac{d\Psi}{dt} = H(t)\Psi(t), \quad (2.1)$$

where H^{TNN} is the tight biding Hamiltonian, which takes into account the coupling between the nearest neighbor atoms only, H^{SOC} is the spin orbit coupling term, and $eF(t).r$ is the pulse-QD interaction term. We first construct a Hamiltonian that include the first two terms and then we add the interaction with the incident pulse.

As we stated in chapter 1, the earlier theoretical studies and the first-principle investigation have shown that the Bloch states in MoS_2 monolayers, near the band edges, consist of Mo d orbitals: d_{z^2} , d_{xy} , and $d_{x^2-y^2}$ orbitals, while the contribution of the S and p orbitals, which form the bonds between Mo and S atoms, is small(33; 34; 35; 36; 37?). Thus, for

calculating the valence and conduction band states within the tight-binding method, a good approximation is to consider only the nearest-neighbor hopping between the three d orbitals. Since d_{xy} and $d_{x^2-y^2}$ orbitals are asymmetric in the plane of Mo atoms, the hopping amplitude between the Mo atoms depends on their relative positions. Since all three orbitals contribute to the formation of the corresponding energy spectra, the hopping between two atoms is described by a 3x3 matrix, whose elements are the hopping integrals. For simplicity, we denote the orbitals as $|\phi_j\rangle$, where $j = 1, 2, 3$ with $\phi_1 = |d_{z^2}\rangle$, $\phi_2 = |d_{xy}\rangle$, and $\phi_3 = |d_{x^2-y^2}\rangle$, then the hopping integrals between the atoms whose relative position is given by the vector R_n are obtained as

$$E_{jj'}(\mathbf{R}) = \langle \phi_j(\mathbf{R}) | H | \phi_{j'}(\mathbf{r} - \mathbf{R}_n) \rangle, \quad (2.2)$$

Where $n = 1 - 6$. However, instead of calculating the hopping integrals for each pair of atoms, we calculate the hopping integrals for one relative orientation of the pair and then calculate the hopping integrals for other orientations from the following expression

$$E_j(g_m \mathbf{R}_n) = D(g_m) E_j(\mathbf{R}_n) D(g_m)^\dagger, \quad (2.3)$$

Where $E_j(g_m \mathbf{R}_n) = [E_{j1}(g_m \mathbf{R}_n) E_{j2}(g_m \mathbf{R}_n) E_{j3}(g_m \mathbf{R}_n)]^T$ and $D(\hat{g}m)$ is a matrix representing symmetry operation $\hat{g}m$ which transforms R_n to R_m . Only a subset of symmetry operations of D_{3h} symmetry group, $\hat{E}, \hat{C}_3, \hat{C}_3^2, \sigma_v^\wedge, \sigma_v^{\wedge'}, \sigma_v^{\wedge''}$ needs to be used in order to transform R-vector from one orientation to the other ones. Here \hat{E} is the identity operation, \hat{C}_3 is the rotation operator by the angle of $\frac{2\pi}{3}$ around the z-axis, and σ_v^\wedge is the reflection operator at a plane perpendicular to the x-y plane, By fitting the results of the tight-binding calculations

to those from the first-principle calculations (38), values of the following hopping integral are obtained

$$E_{11}(\mathbf{R}_1) = t_0 = -0.184 \text{ eV} \quad E_{12}(\mathbf{R}_1) = t_1 = 0.401 \text{ eV}$$

$$E_{13}(\mathbf{R}_1) = t_2 = 0.507 \text{ eV} \quad E_{12}(\mathbf{R}_{22}) = t_{11} = 0.218 \text{ eV}$$

$E_{23}(\mathbf{R}_1) = t_{12} = 0.338 \text{ eV} \quad E_{12}(\mathbf{R}_{33}) = t_{22} = 0.057 \text{ eV}$.(2.4) Also, the on-site energy of d_{z^2} is equal to $\epsilon_0 = 1.046 \text{ eV}$ and both d_{xy} and $d_{x^2-y^2}$ on-site energies are equal to $\epsilon_2 = 1.046 \text{ eV}$. Using the values from Eqs. (2.3) and (2.4), the off-diagonal matrix elements are obtained as follows

$$h(\mathbf{R}_1) = \begin{bmatrix} t_0 & t_1 & t_2 \\ -t_1 & t_{11} & t_{12} \\ t_2 & -t_{12} & t_{22} \end{bmatrix} = h(\mathbf{R}_6)^T,$$

$$h(\mathbf{R}_2) = \begin{bmatrix} t_0 & \frac{1}{2}t_1 - \frac{\sqrt{3}}{2}t_2 & -\frac{\sqrt{3}}{2}t_1 - \frac{1}{2}t_2 \\ -\frac{1}{2}t_1 - \frac{\sqrt{3}}{2}t_2 & \frac{1}{4}t_{11} + \frac{3}{4}t_{22} & -\frac{\sqrt{3}}{4}t_{11} - t_{12} + \frac{\sqrt{3}}{4}t_{22} \\ \frac{\sqrt{3}}{2}t_1 - \frac{1}{2}t_2 & -\frac{\sqrt{3}}{4}t_{11} + t_{12} + \frac{\sqrt{3}}{4}t_{22} & \frac{3}{4}t_{11} + \frac{1}{4}t_{22} \end{bmatrix} = h(\mathbf{R}_4)^T.$$

$$h(\mathbf{R}_3) = \begin{bmatrix} t_0 & \frac{1}{2}t_1 + \frac{\sqrt{3}}{2}t_2 & \frac{\sqrt{3}}{2}t_1 - \frac{1}{2}t_2 \\ -\frac{1}{2}t_1 + \frac{\sqrt{3}}{2}t_2 & \frac{1}{4}t_{11} + \frac{3}{4}t_{22} & \frac{\sqrt{3}}{4}t_{11} - t_{12} - \frac{\sqrt{3}}{4}t_{22} \\ -\frac{\sqrt{3}}{2}t_1 - \frac{1}{2}t_2 & \frac{\sqrt{3}}{4}t_{11} + t_{12} - \frac{\sqrt{3}}{4}t_{22} & \frac{3}{4}t_{11} + \frac{1}{4}t_{22} \end{bmatrix} = h(\mathbf{R}_5)^T.$$

Finally, the diagonal submatrices, which take into account the on-site energies, an external scalar potential, and the spin-orbit coupling (SOC), have the form:

$$\begin{bmatrix} \varepsilon_0 + V(x, y) & 0 & 0 \\ 0 & \varepsilon_2 + V(x, y) & \pm 2i \\ 0 & \mp 2i & \varepsilon_2 + V(x, y) \end{bmatrix}$$

Where the off-diagonal terms take into account the SOC, while the upper sign is for spin-up and the lower sign is for spin-down components. Thus, the Hamiltonian used for calculating the eigenstates of the system is of the following form

$$\begin{bmatrix} h_D & \cdots & h(\mathbf{R}_n) \\ \vdots & \ddots & \vdots \\ h(\mathbf{R}_n) & \cdots & h_D \end{bmatrix}$$

Where each element (block) represents interactions of one atom with other atoms in Mo layer, i.e., off-diagonal terms represent the coupling of the nearest neighbor atoms, and the diagonal terms represent the on-site energies and the SOC interaction. Although the model is applied for MoS_2 , it is also applicable to all transition metal dichalcogenides (e.g., $WS_2, MoSe_2, WSe_2$, etc.) monolayers. The only difference is in the values of the corresponding parameters (lattice constant, on-site energies, and hopping energies). The total tight-binding Hamiltonian includes H^{TNN} and H^{SOC} . Now we can add the $eF(t).r$ term. This term characterizes the interaction of TMDC QDs with ultrashort optical pulses. The duration of the pulse is in a few femtoseconds time range. Assuming that the relaxation in QDs are longer than the duration of the pulse, we describe the electron dynamics in the field of the pulse within the coherent approach, which is described by a single particle

time-dependent Schrödinger equation (TDSE):

$$i\hbar \frac{d\Psi_i(t)}{dt} = H(t)\Psi_i \quad H(t) = H_0 - e\mathbf{F}(t) \cdot \mathbf{r}, \quad (2.5)$$

Where $\mathbf{F}(t)$ is the pulse's electric field, e is an electron charge, \mathbf{r} is the position vector, and wavefunction $\Psi_i(t)$ is a single particle electron wavefunction with initial condition $\Psi_i(t = -\infty) = \phi_i$. Here ϕ_j and $E_j = 1, \dots, 3N_{Mo}$ (for a given spin component) are eigenfunction and corresponding energies of the tight-binding Hamiltonian, H_0 . For an optical pulse, we use the following profile of the electric field

$$F(t) = F_0 \cos(\omega t) e^{-(\frac{t}{\tau})^2}. \quad (2.6)$$

Here τ is the pulse duration, $\omega = 2.3 \frac{rad}{fs}$ is the frequency of the pulse, and F_0 is field amplitude, which is related to the power of the pulse $P = c(F_0)^2/4\pi$, where c is the speed of light. We express the solutions of equation (2.5) in the basis of eigenfunctions of the field-free Hamiltonian, H_0 , as follows

$$\Psi_i(t) = \sum_i \beta_{i,j}(t) \Phi_j \exp(-\frac{i}{\hbar} E_j t). \quad (2.7)$$

Then the expansion coefficients $\beta_{i,j}$ satisfy the following system of differential equations ($j = 1, \dots, 3N_{Mo}$):

$$i\hbar \frac{d\beta_{i,j}(t)}{dt} = \sum_{j'} \mathbf{F}(t) \cdot \mathbf{D}_{j,j'} \beta_{i,j'}(t) \exp[\frac{i}{\hbar} (E_{j'} - E_j)t] \quad (2.8)$$

With initial condition $\beta_{i,i} = 1$ and $\beta_{i,j \neq i} = 0$. Here $D_{j,j'}$ are the dipole matrix elements:

$$\mathbf{D}_{j,j'} = \langle \Phi_j | e\mathbf{r} | \Phi_{j'} \rangle. \quad (2.9)$$

CHAPTER 3

Absorption in Transitional Metal Dichalcogenides

3.1 Introduction:

TMDC monolayers have controllable nonlinear optical properties (39), that can be changed in two ways. First approach is introducing defects and impurities (40). Such impurities can introduce in-gap states (also known as edge states) and modify the band gap of TMDC monolayers. The nonlinear properties of two-dimensional materials can be also enhanced by considering composites of such materials, for example, MoS_2 graphene nanocomposites(41). Such systems have strong absorption and nonlinear response. Combination of a few layers of TMDC (MoS_2) allows to combine saturable absorption and large nonlinear third-order susceptibility of such systems(42). Formation of many-body complexes, such as excitons and biexcitons, in TMDC monolayers and multilayer systems strongly affects their nonlinear optical response (43). Another way to control the optical properties of TMDC monolayers is to lower their dimensionality even more and consider quantum dots (QDs) based on TMDC monolayers. The quantum dots (44; 45) represent an ultimate reduction in the dimensionality of nanoscopic devices. The electrons are confined in all spatial directions and occupy spectrally-sharp energy levels like those found in atoms. The optical properties of QDs are determined by their sizes and shapes. Quantum dots can also support the edge states. In this dissertation we theoretically and computationally investigate interaction of different size of MoS_2 QDs with ultrashort pulse. In the rest of the chapter we will explore the absorption properties and high harmonic generation in TMDC QDs.

3.2 Method:

Population of the excited QD states after the pulse is determined by expansion coefficients $\beta_{i,j}(t = \infty)$. Then the energy absorbed by the QD can be calculated from the following expression

$$W_{abs} = \sum_{s=\uparrow\downarrow} \sum_{i \in VB} \sum_{j=1}^{3N_e} |\beta_{i,j}(t = \infty)|^2 (E_j - E_i) \quad (3.1)$$

Where the first sum is over two components spin, up (\uparrow) and down (\downarrow), and the sum over i is the sum over all occupied initial states of the QD. The absorbance of the QD is determined by the following expression

$$\alpha = \frac{W_{abs}}{A_0 \epsilon_0 c \int_{-\infty}^{\infty} |\mathbf{F}(t)|^2 dt}$$

Where A_0 is the area of QD and ϵ_0 is the dielectric permittivity of the surrounding medium. The absorbance, defined by α , is calculated as part of the energy of the pulse directly incident on the QD, i.e., within the area A_0 of the QD, that is absorbed by the QD. Because the absorbance is defined as the part of the energy of the whole laser pulse with the spot area A_0 that is absorbed by the QD, all values for alpha calculated below should be multiplied by $\frac{A_0}{A_{pulse}}$.

3.3 Results and Discussion:

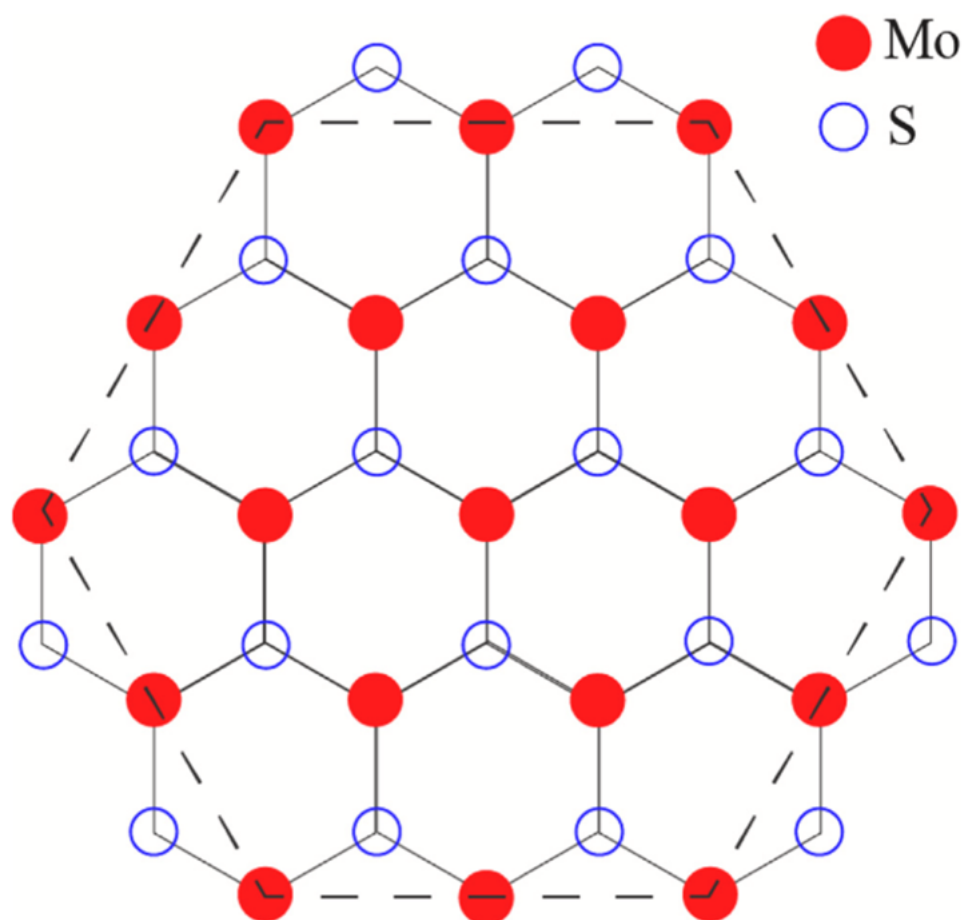


Figure 3.1 Hexagonal MoS_2 quantum dot. It consists of Mo (filled red dots) and S (open dots) atoms. The quantum dot shown in the figure has the size of $N_e = 19$. The dashed line illustrates the hexagonal shape of the quantum dot.

We introduce TMDC quantum dot(QD) as nanopatches of TMDC monolayers of hexagonal shape. The QDs has honeycomb crystal structure, which consists of two sublattices, A and B. The figure 3.1 shows the shape of QD for 19 Mo atom. The size of the QDs is determined by the number of Mo atoms in it. In MoS_2 QDs at each Mo-site there are two S atoms so the number of S atom is twice as the number of Mo atoms. The electron states in such QDs is described within three-band tight bonding model, where coupling happen only between nearest-neighbor of Mo atoms. We considered different sizes of the QDs, 19, 61, and 91. All of them has the same hexagonal shape. The Hamiltonian of TMDC electron system, in the absence of pulse, is the three band tight bonding Hamiltonian, H_0 . For each Mo atom only the three orbital d_{xy} , d_{z^2} , and $d_{x^2-y^2}$ are considered because these orbitals has the most contribution in Fermi level of TMDCs. Such a models for TMDCs gives one valence band and two conduction bands. The number of electrons in the QD is equal to twice the number of Mo atoms, which we also define as size of the QD, N_{Mo} . Spin-orbit interaction is also considered by three band tight binding model.

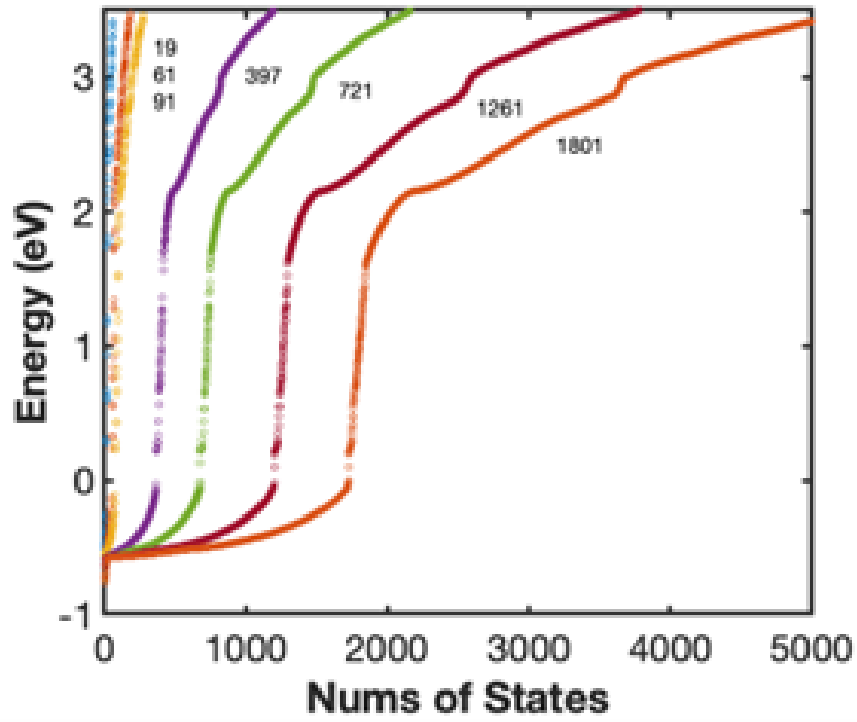


Figure 3.2 Energy spectra of MoS_2 QD of sizes $N_e = 19, 61, 91$. The inset shows the size of the band gap vs N_e . As QD size increase the band gap decreases.

The energy spectrum of TMDC QDs are shown in the figure 3.2 for different sizes $N_{Mo} = 19 - 1801$. As the size of QDs increases the band gap decreases from 2.3 eV for QD $N_{Mo} = 19$ to 1.95 eV for $N_e = 1801$. This is consistent with other experimental and theoretical results as size of the QDs increases its properties should get close to MoS_2 monolayer properties, the band gap for MoS_2 monolayer is 1.8 eV.

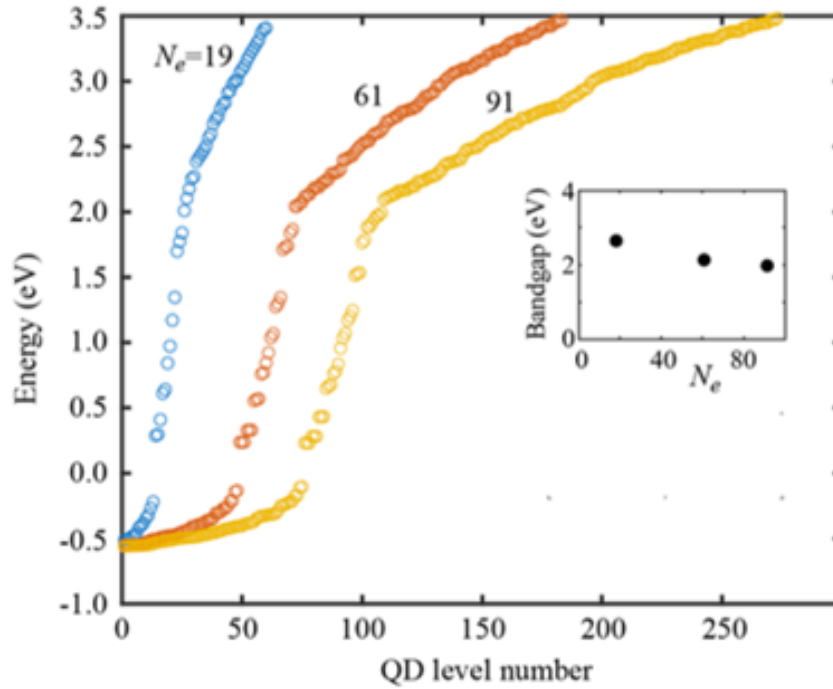


Figure 3.3 Energy spectra of MoS_2 QD of sizes $N_{Mo} = 19, 61, 91$. The inset shows the size of the band gap vs N_{Mo} . As QD size increase the band gap decreases.

Figure 3.3 shows the energy spectrum more clear for small QD sizes, $N_{Mo} = 19, 61, 91$. For all sizes we see the in-gap states which also called edge states. These edge states close bulk band gap and act as absorption channel in undoped MoS_2 and increase the overall absorption. For MoS_2 monolayer, the bandgap is around 1.8 eV. The inset shows the inverse relation between band gap size versus size of QD at small sizes.

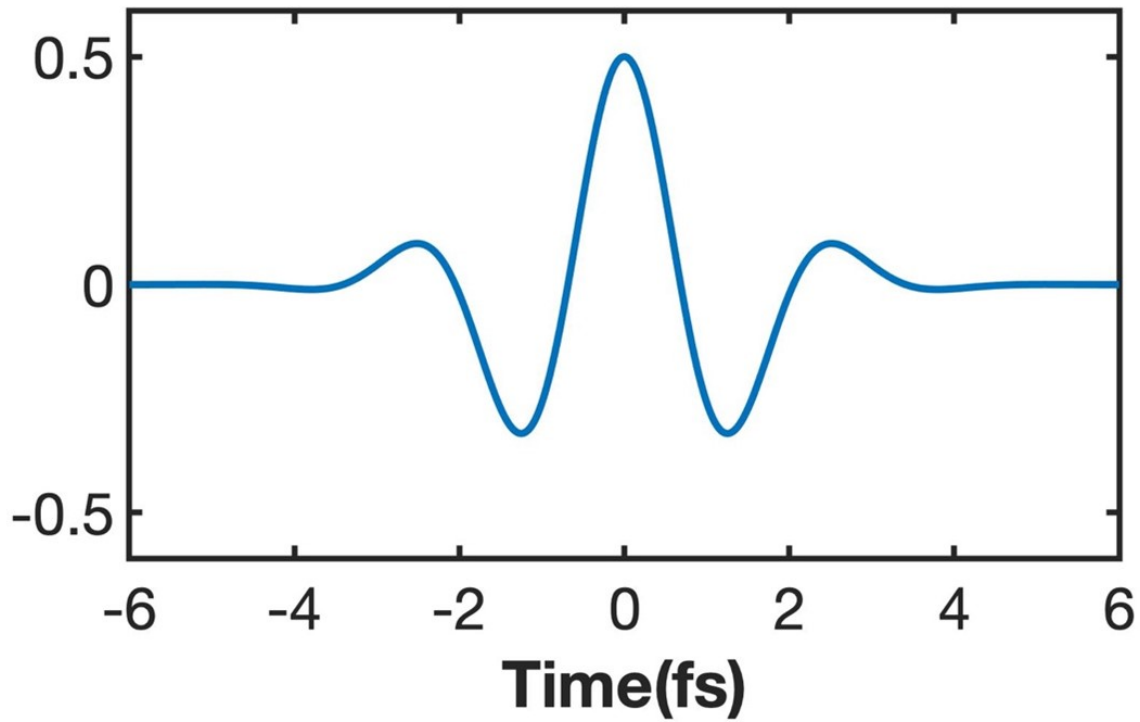


Figure 3.4 shows the electric field of an optical pulse vs time(femtosecond) for one oscillation.

Figure 3.4 indicating the electric field profile of the pulse versus time for $\omega = 2.3\text{rad/fs}$, $F_0 = 0.5\text{V/\AA}$. The energy of an optical pulse is determined by two factors: first one is the frequency of the pulse, i.e. $\hbar\omega$, and the second one is determined by the amplitude of the pulse, F_0 , which introduces an energy scale of the order of a_0F_0 . Here $a_0 \sim 3.16\text{\AA}$ is lattice constant in MoS_2 monolayers.

At small amplitude absorbance is highly sensitive to frequency(or wavelength λ) of the pulse. This property is illustrated in figure 3.5 where the absorbance for $N_{Mo} = 19$ and 61 QD is shown as a function of F_0 for three different values of λ . For the field amplitude less than $\sim 0.75V/\text{\AA}$ absorbance has strong dependence on the wavelength, λ , where absorbance varies from 2% (at $\lambda = 820$ nm) to 25% (at $\lambda = 400$ nm). At large field amplitude, $F_0 > 0.75V/\text{\AA}$, the absorbance almost does not depend on λ . This shows the property that at large F_0 the main energy scale of the pulse is determined by electric field of the pulse, which mixes almost all states of the QD and results in that absorbance is independent of λ .

At small field amplitude, the absorbance mainly decreases with the field amplitude, i.e. shows saturable behavior, see figure 3.5 for the wavelength 400 nm and 600 nm. These wavelengths correspond to the frequencies of $3eV$ and $2.0eV$, which are above or close to the bandgap of MoS_2 monolayer. When the wavelength becomes large, i.e. the corresponding frequency of the pulse is less than the bulk bandgap, the absorbance increases with the field amplitude, F_0 , the data for $\lambda = 820$ nm (energy is $1.5eV$) shown in figure 3.6. When the frequency of the pulse is less the bulk bandgap, the edge states provide the main contribution to the absorbance of TMDC QDs at small pulse amplitudes. With increasing the field amplitude, F_0 the absorbance becomes less sensitive to the frequency of the pulse.

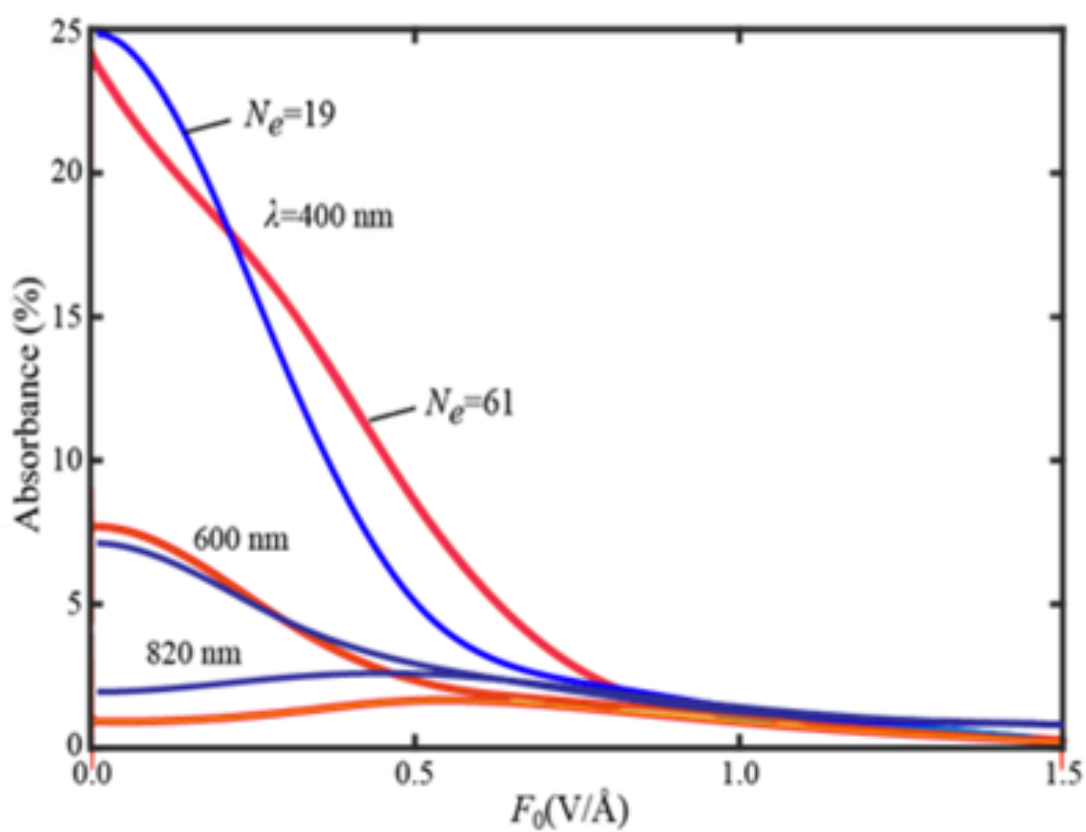


Figure 3.5 Absorbance as a function of the pulse amplitude. The duration of the pulse is $\tau = 2fs$. The results are shown for three different wavelengths: $\lambda = 400nm, 600nm$, and $820nm$. The size of MoS_2 QD is $N_{Mo} = 19$.

In figure 3.6 the absorbance is shown as a function of the wavelength of the pulse for the amplitude of $F_0 = 0.5V/\text{\AA}$. The absorbance varies from 2% to 5% with nonmonotonic dependence on λ . The maximum absorbance is at small λ , i.e., large frequency, which is correlated with the resonant conditions between the bulk states of the QD. We analyze in more details the case of a large wavelength, $\lambda = 820\text{nm}$, i.e. small frequency of 1.5eV. For such small frequency, the edge states plays a more important role.

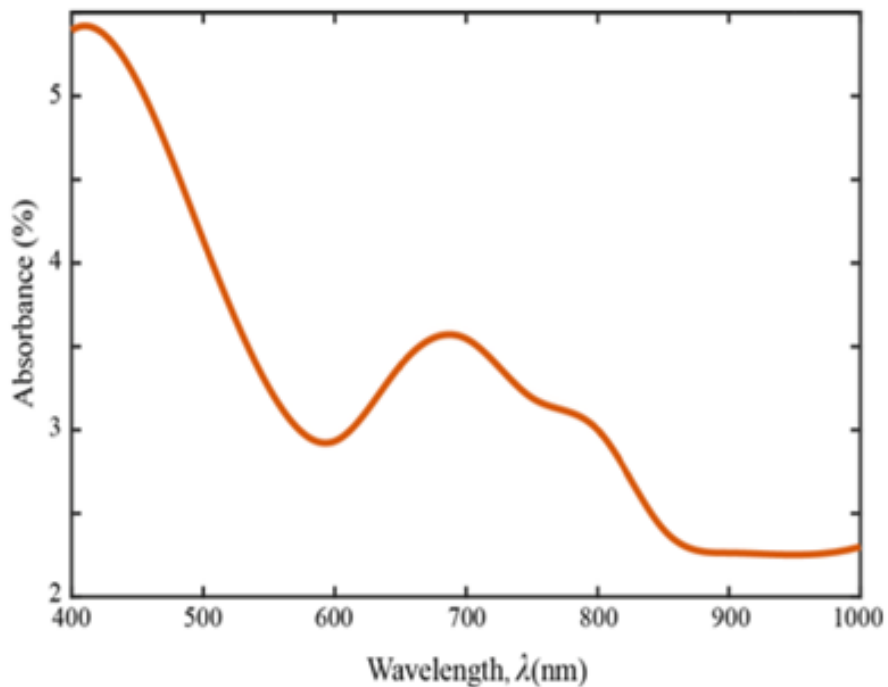


Figure 3.6 Absorbance as function of wavelength of the optical pulse. The amplitude of the pulse is $F_0 = 0.5V/\text{\AA}$ and its duration is $\tau = 2fs$. The sizes of MoS_2 QD are $N_{Mo} = 19$.

The absorbance as a function of the field amplitude for TMDC QDs of different sizes and for different duration of pulse, τ is shown on figure 3.7. As size of QD, increases the absorbance decreases. For example, for $N_{Mo} = 19$ the maximum absorbance is around 3%, while for $N_{Mo} = 91$, the maximum absorbance is around 2.2%. This is because with increasing N_{Mo} , the relative number of the edge states compared to the bulk states decreases.

As τ increases the pulse becomes more localized in the frequency domain. Consequently the excitation of the high energy levels of the QD become suppressed and, as a result, the absorbance decreases with τ . This behavior is shown in the figure 3.7, as τ increase from 2 fs to 4 fs, the absorbance decreases by almost 1%. Such sensitivity to τ is more pronounced at large field amplitudes. The absorbance as a function of field amplitude shows a non-monotonic dependence with a maximum at the amplitude of $F_0 \sim 0.5V/\text{\AA}$, see figure 3.7. The position of the maximum has weak dependence on the size of the QD. The origin of the maximum is because of finite number of the QD states and correspondingly to saturation of population of the high energy levels of the QD. To explore this, in figure 3.7 we calculated the residual population of the QD levels, the population of the QD levels after the pulse. The results are shown for two sizes of $N_{Mo} = 19$, and 61.

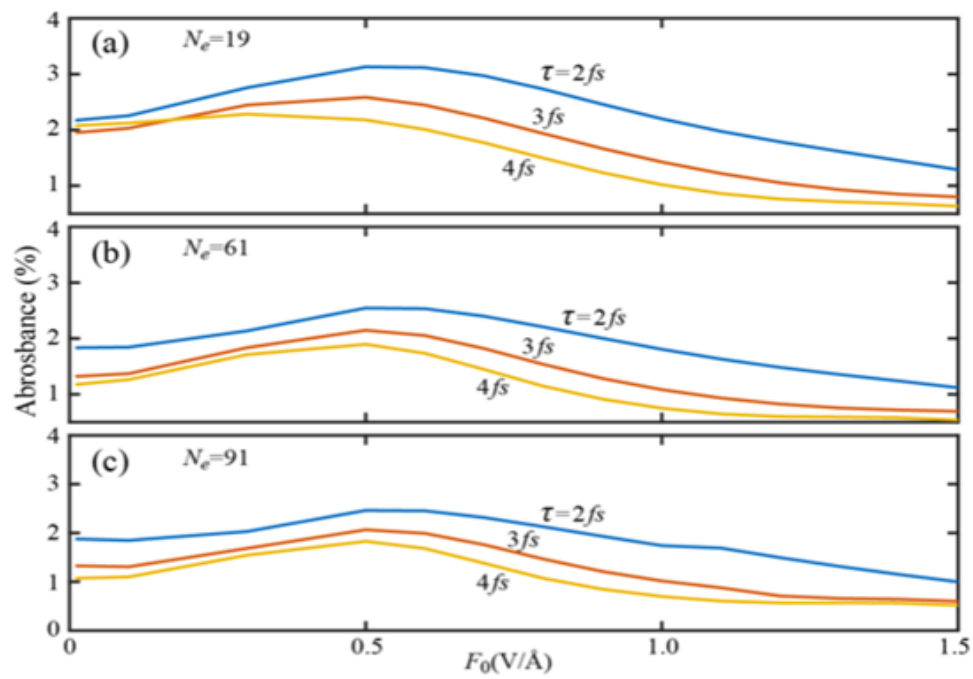


Figure 3.7 Absorbance as a function of the field amplitude, F_0 . The wavelength of the pulse is 820 nm. The absorbance is shown for the three duration of the pulse: $\tau = 2fs$, $3fs$, and $4fs$. The size of MoS_2 QD is (a) $N_{Mo} = 19$, (b) $N_{Mo} = 61$, and (c) $N_{Mo} = 91$.

At small field amplitude, $F_0 = 0.1V/\text{\AA}$, the edge states with the energies less than $2eV$ are mainly populated, see figure 3.8 (a) and (d). Before the pulse only the valence bands are populated and as field amplitude increases more states become populated and around $F_0 \sim 0.5V/\text{\AA}$, all conduction bands states QD, becomes equally populated. That is the field amplitude at which the absorbance reaches its maximum. As we can see in figure 3.8, with further increasing of F_0 , the population of high energy levels increases, but they are still almost equally populated, see figure 3.8 (c), (g). So the absorbance decreases at large amplitude of the optical pulse.

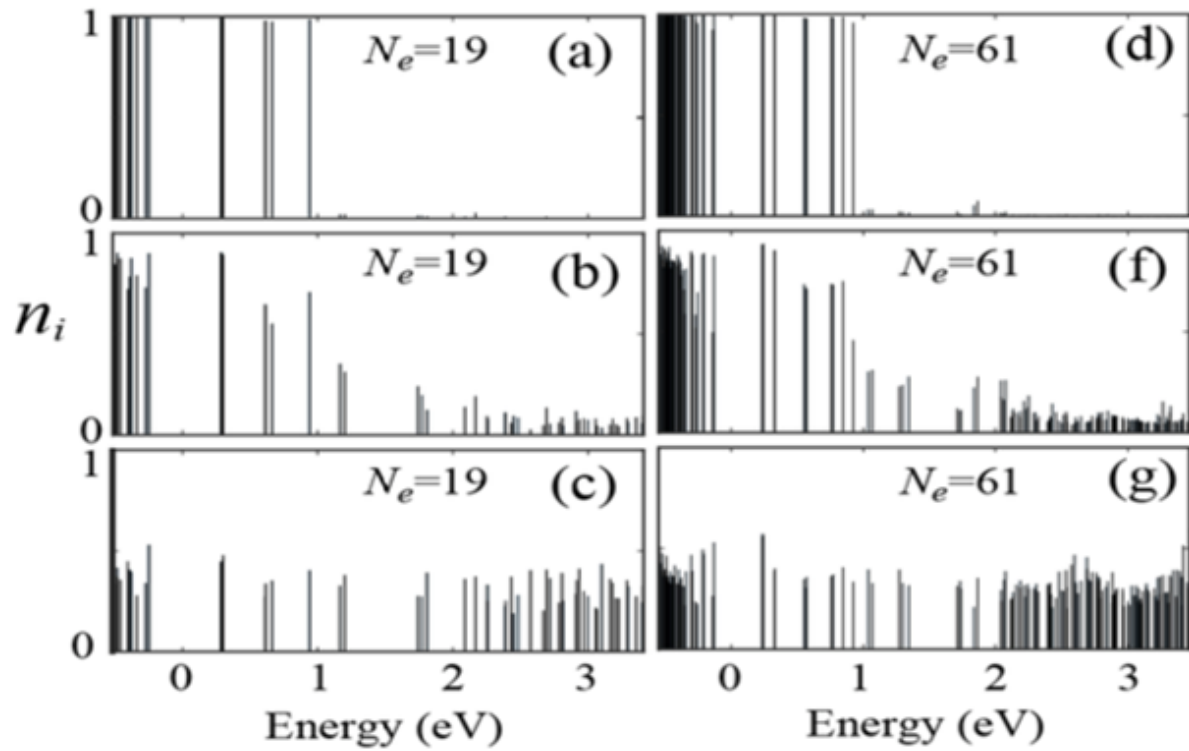


Figure 3.8 Residual population, i.e., population after the pulse, of the QD levels. The wavelength of the pulse is 820 nm and its duration is $\tau = 2fs$. The pulse amplitude is (a) and (d) $F_0 = 0.1V/\text{\AA}$; (b) and (f) $F_0 = 0.5V/\text{\AA}$; (c) and (g) $F_0 = 1.5V/\text{\AA}$. The size of the QD is (a), (b), (c) $N_{Mo} = 19$; (d), (f), (g) $N_{Mo} = 61$.

There is a correlation between the nonmonotonic dependence of the QD absorbance and the pulse amplitude and the population of the high energy levels (conduction bands) of the QDs and is determined by finite number of levels in QDs. Such dependency has been also reported for graphene QDs (11) and is universal property of the finite size QDs. To explain this universal property we calculate absorbance of QDs of different TMDC materials: $MoTe_2$, WTe_2 , $MoSe_2$, WSe_2 , MoS_2 , WS_2 . We took the parameters for calculation from (22). Figure 3.9 shows the results. The absorbance at low field amplitude, less than $F_0 < 0.5V/\text{\AA}$, is strongly depends on the type of materials of the QD. It is correlated to the bulk band gap of the corresponding TMDC: the smaller the band gap the larger the absorbance. For example, $MoTe_2$ has the smallest band gap around 2.0 eV and the largest absorbance, while WS_2 has the largest band gap, ~ 3 eV, and the smallest absorbance. The inset of figure 3.9 shows the corresponding bandgaps of different TMDC materials. The absorbance of the QDs show universal behavior and at large fields reaches the value of $\sim 2\%$. This value depends on the parameters of the pulse, such as its duration, but not on the type of material of the QD. At large pulse amplitude almost all QD levels are equally populated, which is consistent with results in figure 3.8.

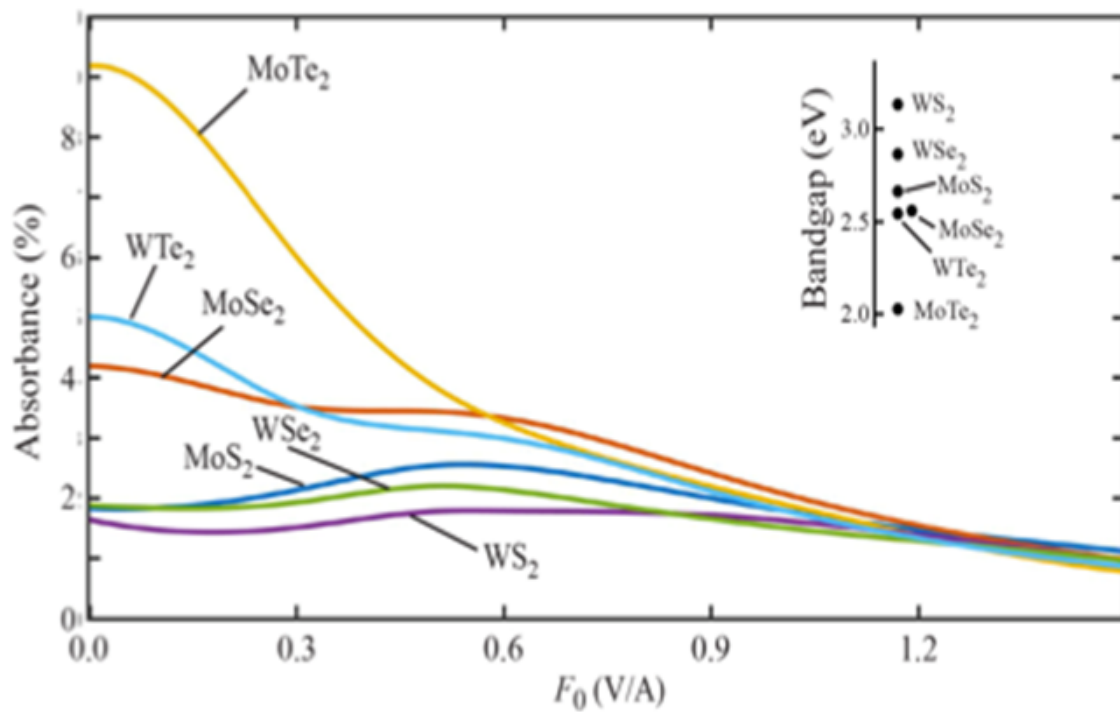


Figure 3.9 absorbance as function of the field amplitude, F_0 . The wavelength of the pulse is 820 nm and the durations of the pulse is $\tau = 2fs$. The size of the QD is $N_{Mo} = 61$. The TMDC materials are labeled next to the corresponding lines. The inset shows the bulk bandgaps of the corresponding materials.

3.4 Conclusion:

As the size of MoS_2 QDs increases their band gap decreases and get close to monolayer band-gap size. All QDs shows in-gap edge states that opens a new channel and increase the overall absorption. When field amplitude increases the absorption would decrease sharply at low field amplitude and then converge to certain amount for different wavelength. Absorbance versus wavelength shows a very sensitive and nonmonotonic behavior. At low wavelength it shows a maximum which is correlated to resonance between bulk states of QD and then it decreases as wavelength increases. At high wavelength, lower pulse energy, the edge state plays major role. As size increases the from 19 to 91 the maximum absorbance would decrease from %3 to %2.2 due to number of edge states relative to bulk states would decrease as size increases. At lows field amplitudes only states lower than 2 eV is populated and at mid amplitude, 0.5 V/A all states valence bands and conduction bands becomes equally populated and with further increasing pulse amplitude the population in conduction bands increases but its rate is less than in rate increase in pulse energy with increasing amplitude. This explains the maximum absorbance at mid field amplitudes. We calculated the absorbance for different type of TMDC materials and there was a correlation between size of the band-gap and absorbance level. For $MoTe_2$ that has the smallest band gap, around 2.0 eV, has the largest absorbance, while WS_2 has the largest band gap, $\sim 3eV$, and the smallest absorbance. The absorbance of the QDs shows a universal behavior and at large fields such that it converges to certain value, %2, and this value does not depend on type of QD and only depend on pulse characteristic such as duration. The result in figure 3.8 that shows all

energy level approximately equally populated confirm this universal behavior.

CHAPTER 4

High Harmonic Generation:

4.1 Introduction:

High harmonic generation (HHG) is a non-linear process during which a target (gas, plasma, solid or liquid sample) is illuminated by an intense laser pulse. Under such conditions, the sample emits the high harmonics of the generation beam. Due to the coherent nature of the process, high harmonics generation is a prerequisite of femtosecond and attosecond physics. The first high harmonic generation was observed in 1977 in the interaction of intense CO_2 laser pulses with plasma generated from solid targets. HHG in gases, was first observed by Mc Pherson and colleagues in 1987, and later by Ferrya et. al. in 1988. High harmonic generation strongly depends on the driving laser field and as a result, the harmonics have similar temporal and spatial coherence properties. High harmonics are generated with the pulse durations shorter than that of the driving laser. This is due to the non-linearity of the generation process, phase-matching conditions, and additional ionization. Often harmonics are emitted co-linearly with the driving laser and can have a very tight angular confinement, sometimes with less divergence than that of the fundamental field and near Gaussian beam profiles.

To observe the high harmonics in solids, which are generated by a short optical pulse, the intensity of the pulse should be relatively large, with the corresponding amplitude that is comparable to internal electric fields in solids. Such strong and short pulses were intensely used to control the transport and optical properties of solids. Such control is determined by

ultrafast nonlinear electron dynamics in the field of pulse. The nonlinear electron dynamics and correspondingly the generation of high harmonics can be tuned by changing the band gap of the material, the level of the internal disorder, and also by changing the dimensionality of a solid going from 3D, to 2D, then to 1D, and finally to zero-dimensional systems. Below we consider the nonlinear optical properties of TMDCs QDs with the hexagonal shape. We characterize the nonlinear optical response of such QDs in terms of nonlinear radiation spectra.

4.2 Method:

By solving the time dependent Schredinger equation, We calculated the charge distribution during the pulse at each atomic position using the population coefficients for the QD levels. As explained in previous chapters, each Mo atom contributes three d orbital, i.e., three energy levels. Then the charge density at each atomic position is the sum of the electron populations of the three energy levels of that atom. For calculating the dipole moment of a QD, we take the center of the QD as $[0,0]$ reference position and calculate the position of each atom with respect to the center. Then the x and y components of the dipole moments are given by the following expressions

$$P_x(t) = Q_1|\beta_1(t)|^2R_{1x} + Q_2|\beta_2(t)|^2R_{2x} + Q_3|\beta_3(t)|^2R_{3x} + \dots$$

$$P_y(t) = Q_1|\beta_1(t)|^2R_{1y} + Q_2|\beta_2(t)|^2R_{2y} + Q_3|\beta_3(t)|^2R_{3y} + \dots(4.1)$$

Where P_x and P_y are the x and y components of the dipole moment of the quantum dot, R_{ix} and R_{iy} are the x and y coordinates of the position vector of the i^{th} atom, and Q_i is the charge of the corresponding atom. With the known dipole moment as a function of time, the radiation spectra of a TMDC QD is calculated as follows

$$I = \frac{Z\omega^4}{12\pi v^2} |P_\omega|^2, \quad (4.2)$$

where P_ω is the frequency Fourier transform of the dipole moment.

4.3 Results and Discussion:

Figure 1. (b) shows the dipole moment of MoS_2 QD when a linearly polarized pulse with the polarization along the x-direction is applied. The generated dipole moment has a nonzero value after the pulse, which is due to nonreversible electron dynamics during the pulse. Also, since the x-axis is not the axis of symmetry of the system, both the x- and y-components of the dipole moment are generated.

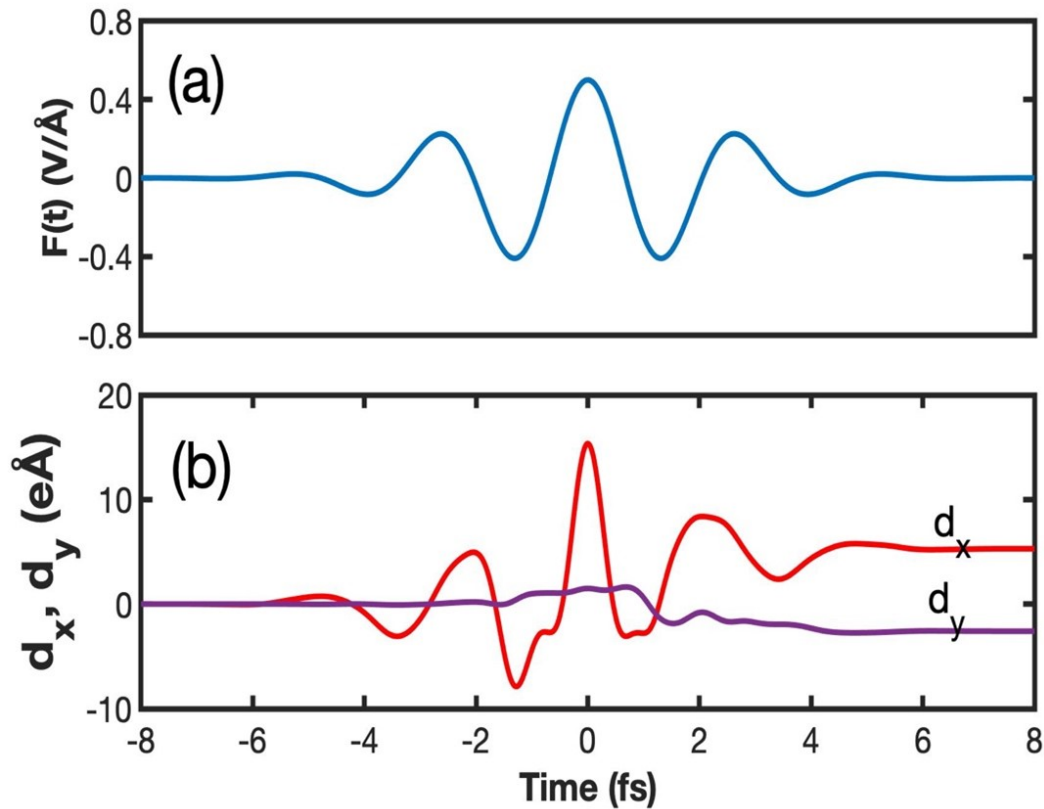


Figure 4.1 (a) electric field of the incident pulse as the function of time. The pulse is linearly polarized in the x-direction. (b) The generated dipole moment of a TMDC QD. Here both the x and y components of the dipole moment are generated. The electron dynamics in the field of the pulse is nonreversible, which is visible as a non-zero residual dipole moment.

Figure 4.2 shows the radiation spectra for the pulse linearly polarized along the x-direction. As the field amplitude increases both the intensity and number of generated high-order harmonics increase. When the field amplitude increases the energy of the pulse increases and consequently more QD energy levels would be involved in the process of generation of high-order harmonics.

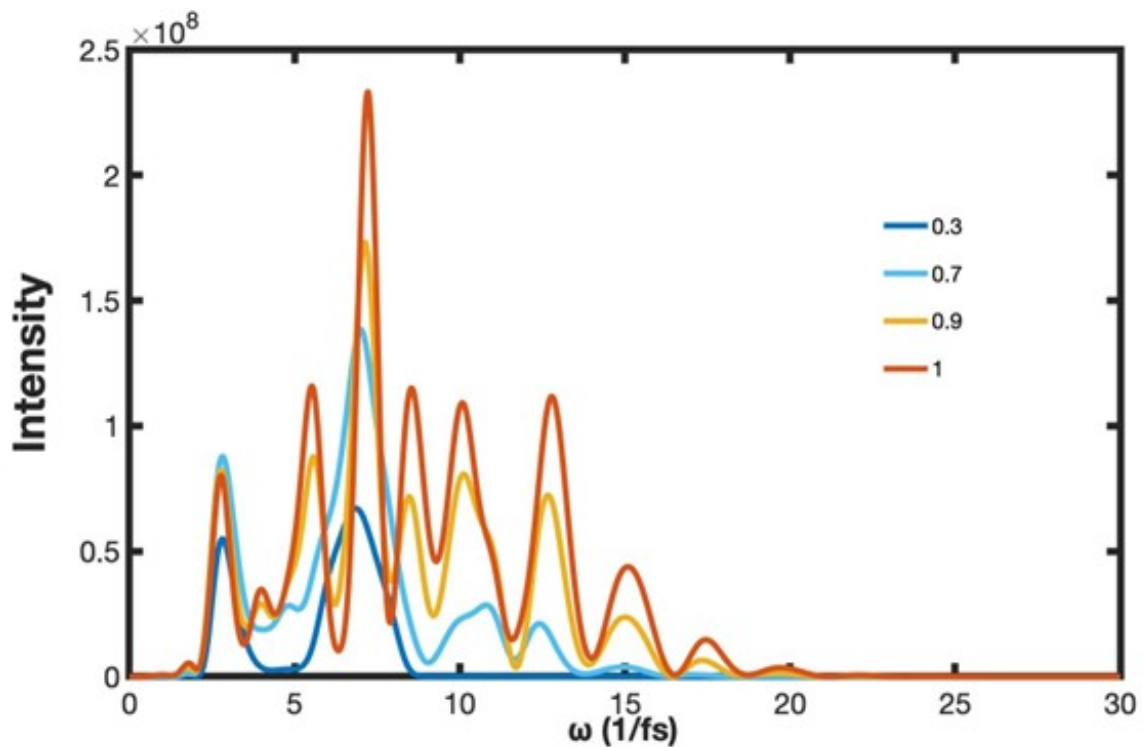


Figure 4.2 Radiation spectra of a TMDC QD as a function of frequency. The pulse is linearly polarized along the x-direction. The amplitude of the pulse is shown next to each line.

Figure 4.3 shows the radiation spectra in semi-logarithmic scale for the incident pulse with different amplitudes in the range of 0.3-1 V/Å. The results are shown for different durations of the pulse and different QD sizes. Here, in Fig. 4.3 (a), (b), and (c), the duration of the pulse is $\tau = 2, 3,$ and 4 fs and the hexagonal TMDC QD consists of 19 Mo atoms, i.e., $N_{Mo} = 19$. In Fig. 4.3(d), (e) and (f), the duration of the pulse is $\tau = 2, 3,$ and 4 fs, respectively, and the number of Mo atoms in the QD is 61, $N_{Mo} = 61$. In Fig. 4.3(g), (h) and (I), the number of Mo atoms is 91, $N_{Mo} = 91$. The results clearly show that with increasing the field amplitude the number of generated high harmonics increases. In all cases, the high-order harmonics have well-pronounced peaks.

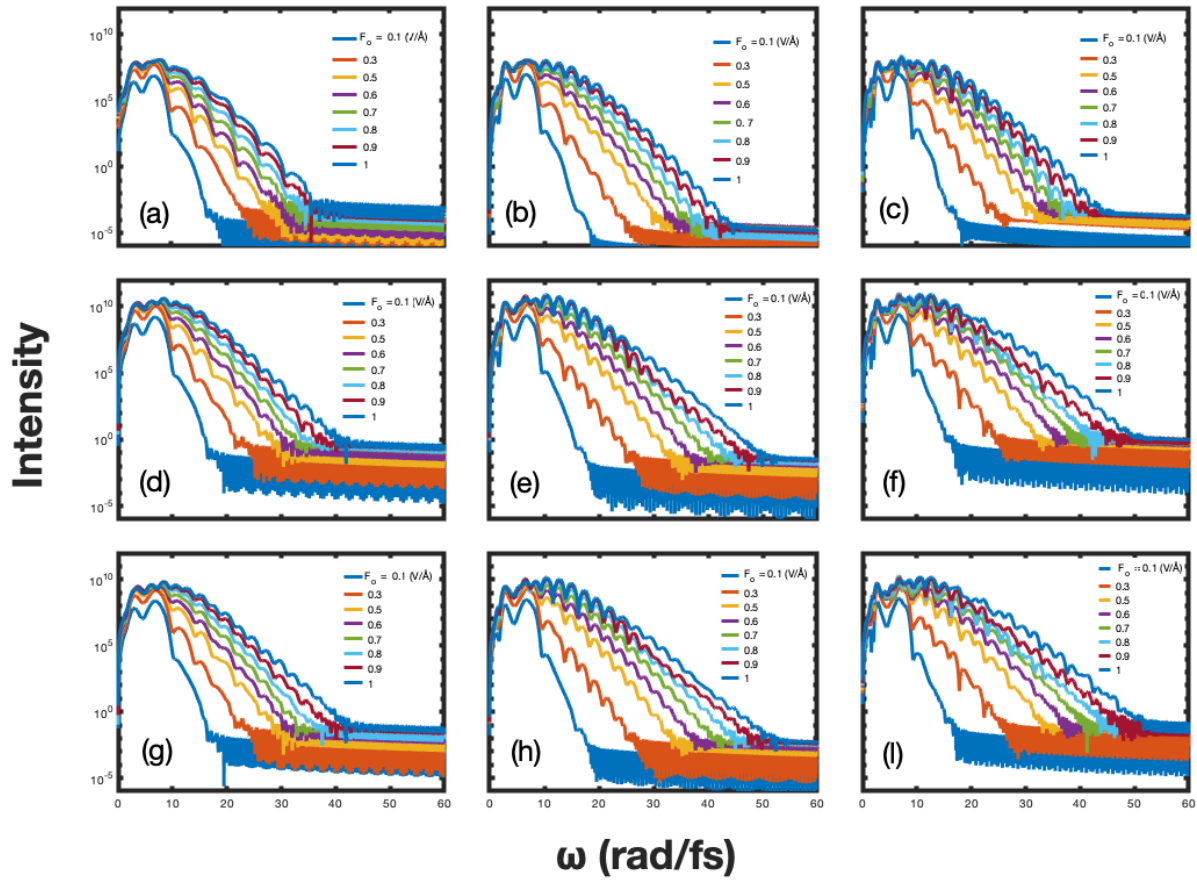


Figure 4.3 Radiation spectra of MoS₂ QD in the field of a linearly polarized pulse. The pulse is polarized along the x -direction. The duration of the pulse and size of a QD, i.e., the number of Mo atoms in QD are the following: (a)-(c) $N_{Mo} = 19$ and the duration of the pulse is $\tau = 2$ fs (a) 3 fs (b), and 4 fs (c); (d)-(f) $N_{Mo} = 61$ and the duration of the pulse is for $\tau = 2$ fs (d) 3 fs (e) and 4 fs (f); (g)-(I) $N_{Mo} = 91$ and the duration of the pulse is $\tau = 2$ fs (g) 3 fs (h), and 4 fs (I). The amplitude of the pulse is marked in each panel. The frequency of the pulse is 2.3 rad/fs.

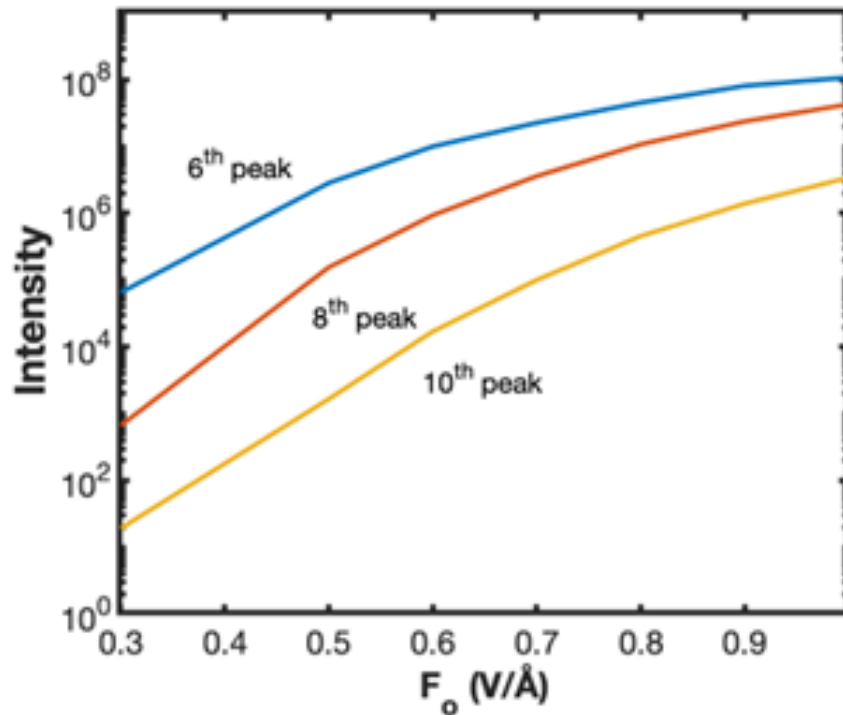


Figure 4.4 The intensities of high-order harmonics (the 6th, 8th, and 10th harmonics) as a function of the field amplitude. The pulse is linearly polarized in the x -direction. The hexagonal MoS₂ QD consists of 61 Mo atoms. The duration of the pulse is 2 fs and its frequency is 2.3 rad/fs.

One of the characteristics of radiation spectra of a TMDC QD, is the intensity of high-order harmonics. In Fig. 4.4, the intensity of the 6th, 8th, and 10th harmonics are shown as a function of the field amplitude of the pulse. The intensities of the corresponding harmonics monotonically increases with the field amplitude showing a saturated behavior at large amplitudes.

Another important characteristic of the generated spectra is the cutoff frequency, i.e., the largest harmonic that is generated. The cutoff frequency is shown in Fig. 4.5 as a function of the field amplitude for different QD sizes and different durations of the pulse. The number of generated high harmonics increases with increasing the field amplitude. The dependence on the field amplitude is almost linear with the fastest dependence at the low amplitudes. When the duration of pulse, τ , increases from 2 fs to 3 fs, the number of generated high harmonics sharply increases, but when τ changes from 3 fs to 4 fs the cutoff frequency remains almost the same for most of F_0 values.

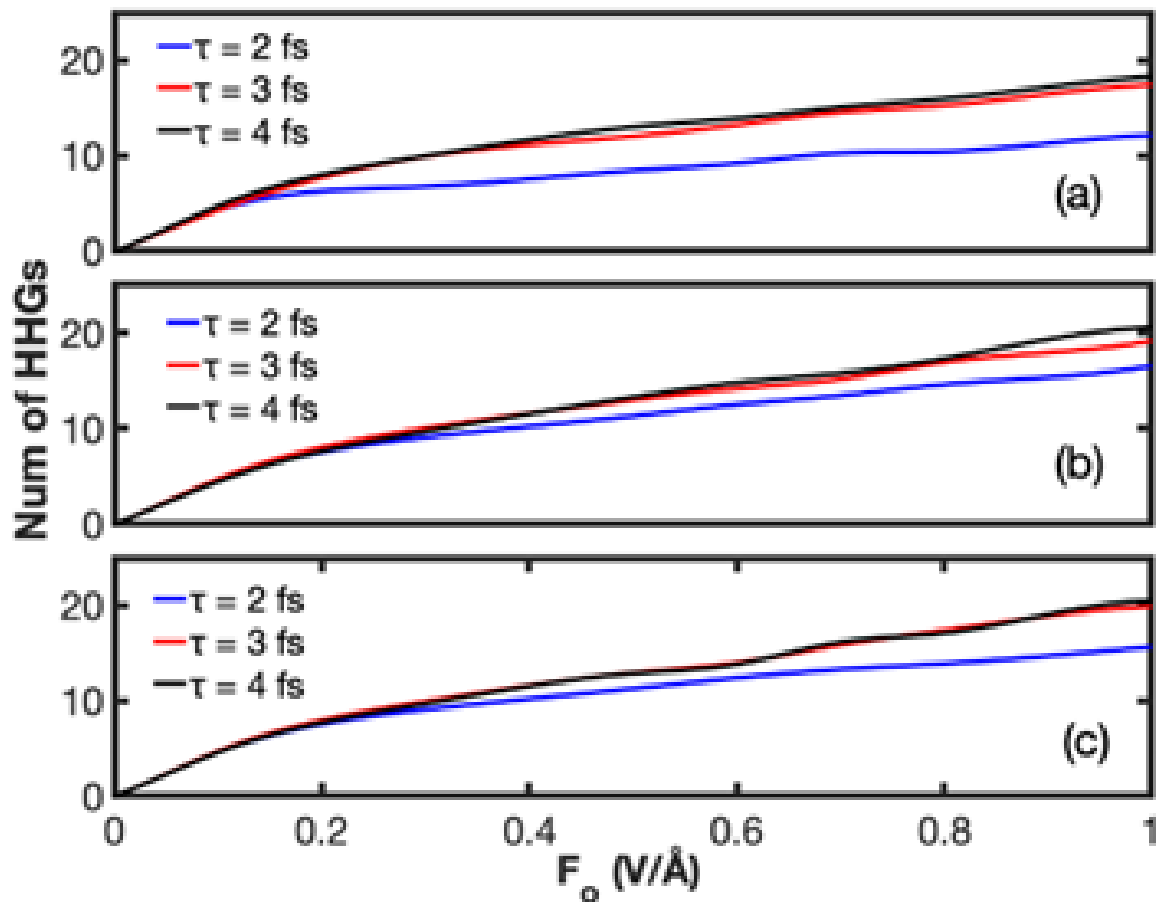


Figure 4.5 Cutoff frequency as a function of the field amplitude. The QD size, i.e., the number of Mo atoms, is $N_{Mo} = 19$ (a), 61 (b), and 91 (c). The duration of the pulse is marked at each panel. The frequency of the pulse is 2.3 rad/fs.

The generated radiation spectra also depend on the frequency of the pulse. Such dependence is illustrated in Fig. 4.6, where the cutoff frequency versus field amplitude is shown for different values of ω . The cutoff frequency monotonically increases with the field amplitude, F_0 , for all values of the pulse frequency, ω . Also the cutoff frequency increases as ω increases. This is because there are more oscillation with higher ω which leads to higher number of high harmonics. The cutoff frequency monotonically increases with the frequency of the pulse, but such a dependence is not linear, and in the units of the frequency of the pulse, the number of high harmonics decreases with ω . Namely, for example, for the field amplitude of 1 V/\AA , the largest frequency that can be generated for $\omega = 1 \text{ rad/fs}$ is around 25 rad/fs , which correspond to the maximum harmonic order of around 25, while for the frequency of the pulse of 4.18 rad/fs , the frequency of the largest harmonics is around 40 rad/fs , which corresponds to the maximum harmonic order of around 10.

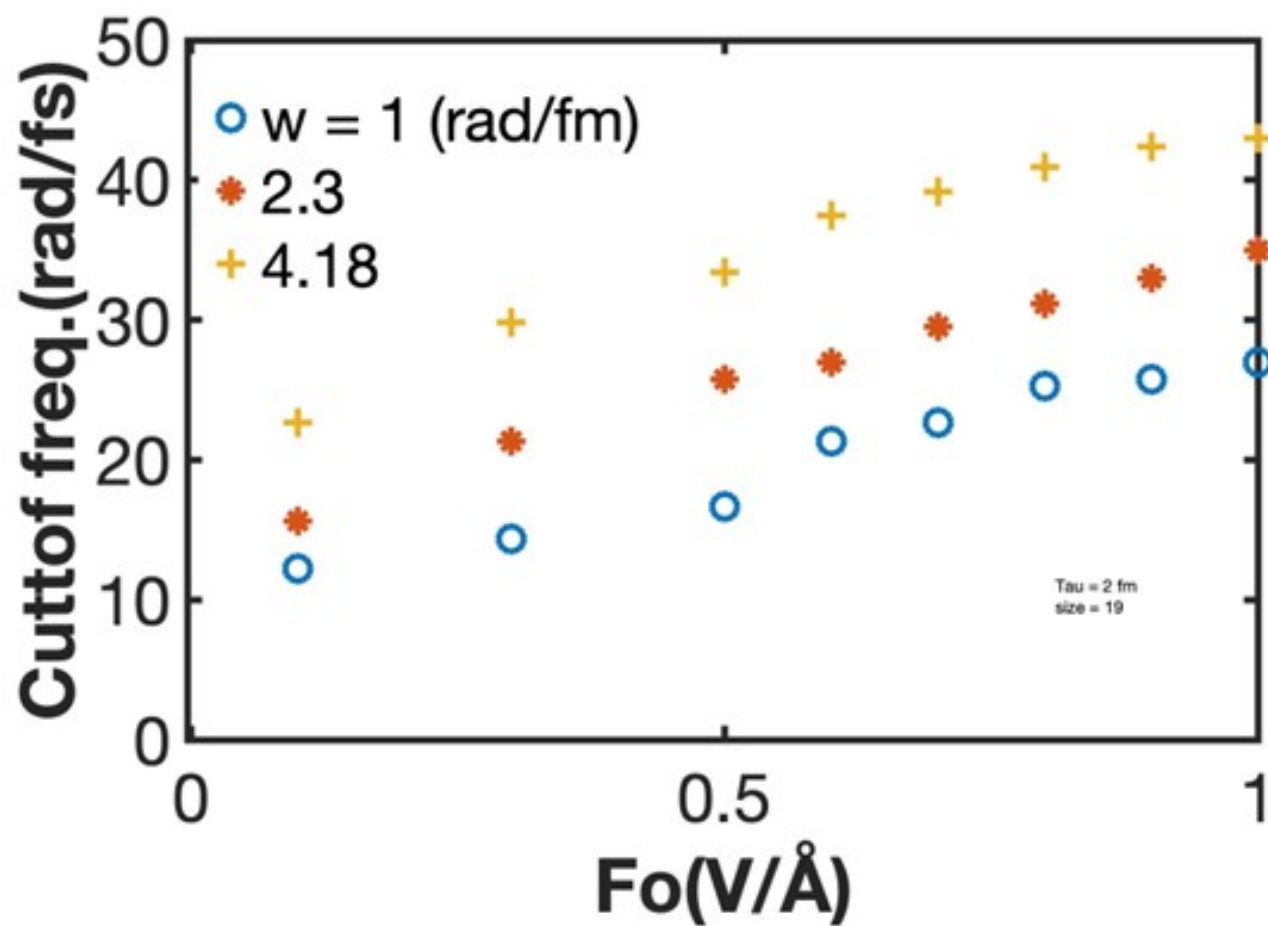


Figure 4.6 Cutoff frequency versus the field amplitude for different values of the frequency of the pulse, ω . The QD size is 19, i.e., the QD consists of 19 Mo atoms. The pulse duration is 2 fs.

Important characteristics of the radiation spectra is how the cutoff frequency depends on the QD size. Such a dependence is shown in Fig. 4.7, where the cutoff frequency is shown for three QD sizes. We see that the QD with the size of 61, i.e., consisting of 61 Mo atoms, has the highest cutoff frequency, which suggests that the most efficient generation of high-order harmonics is realized at the intermediate QD sizes around 61. This is because as the QD size increases the number of levels increases so the number of high harmonics or cutoff frequency should also increase with the size, but with increasing the number of energy levels the energy difference between the levels decreases and energy spectrum shows more continuous behaviour suppressing the nonlinear effects, which compensate or has stronger effect than the effect of the larger number of levels.

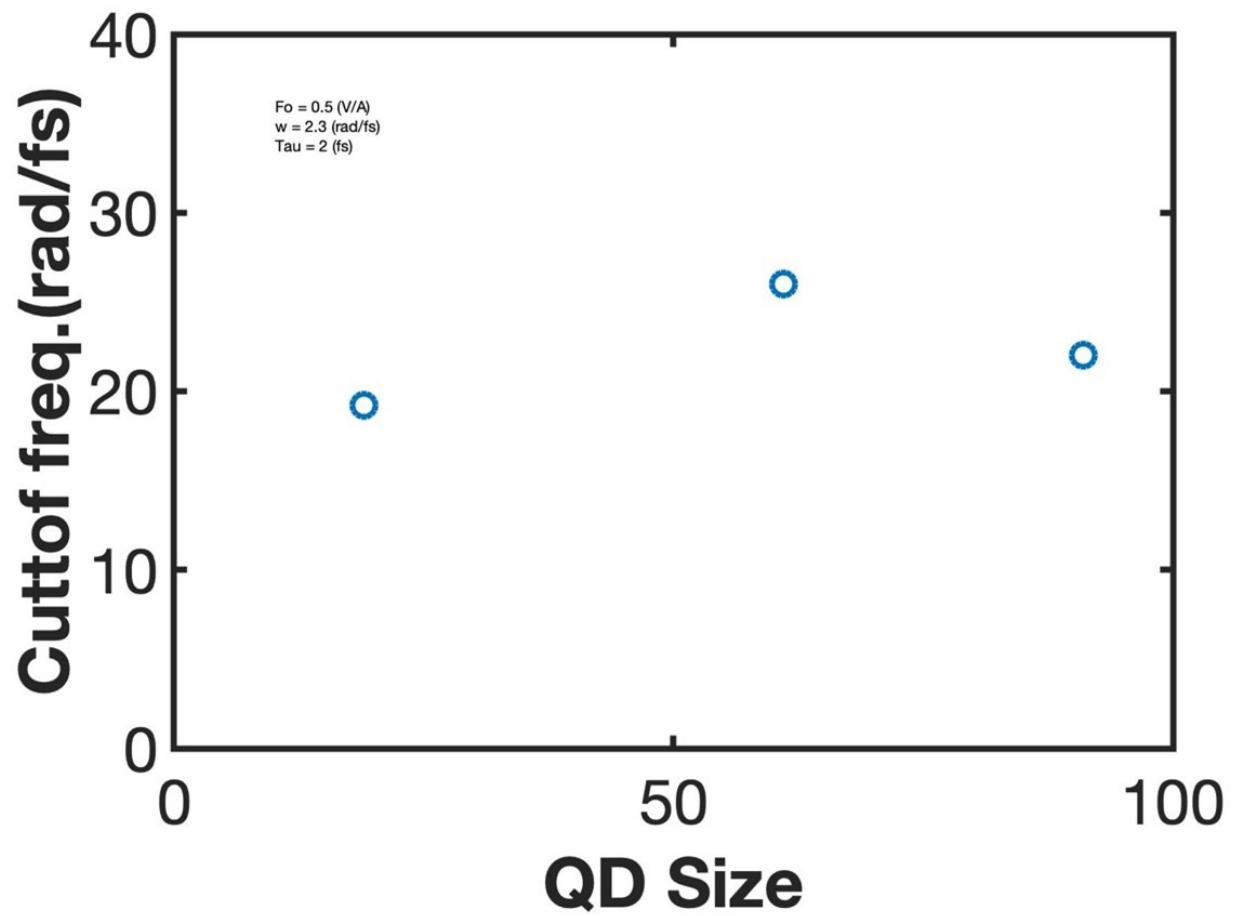


Figure 4.7 Cutoff frequency versus a QD size. The amplitude of the pulse is $F_0 = 0.5V/A$, its frequency is $\omega = 2.3$ rad/fs, and its duration is $\tau = 2$ fs.

The dependence of the radiation spectrum on the QD size is also illustrated in Fig. 4.8, where the intensity of the 5th harmonic is shown for different QD sizes. The intensity of the corresponding harmonic is the largest for the QD consisting of 61 Mo atoms, which is visible for all field amplitudes. Realization of the intensity maximum at intermediate QD size can be explained by the same reasoning as presented above. Namely, that with increasing the QD size the number of single-particle levels increases, which effectively increases the intensity of the generated harmonics, while the interlevel energy difference decreases, which makes energy spectrum more continuous and suppresses the generation of high harmonics. The second factor would compensate the effect of the first one.

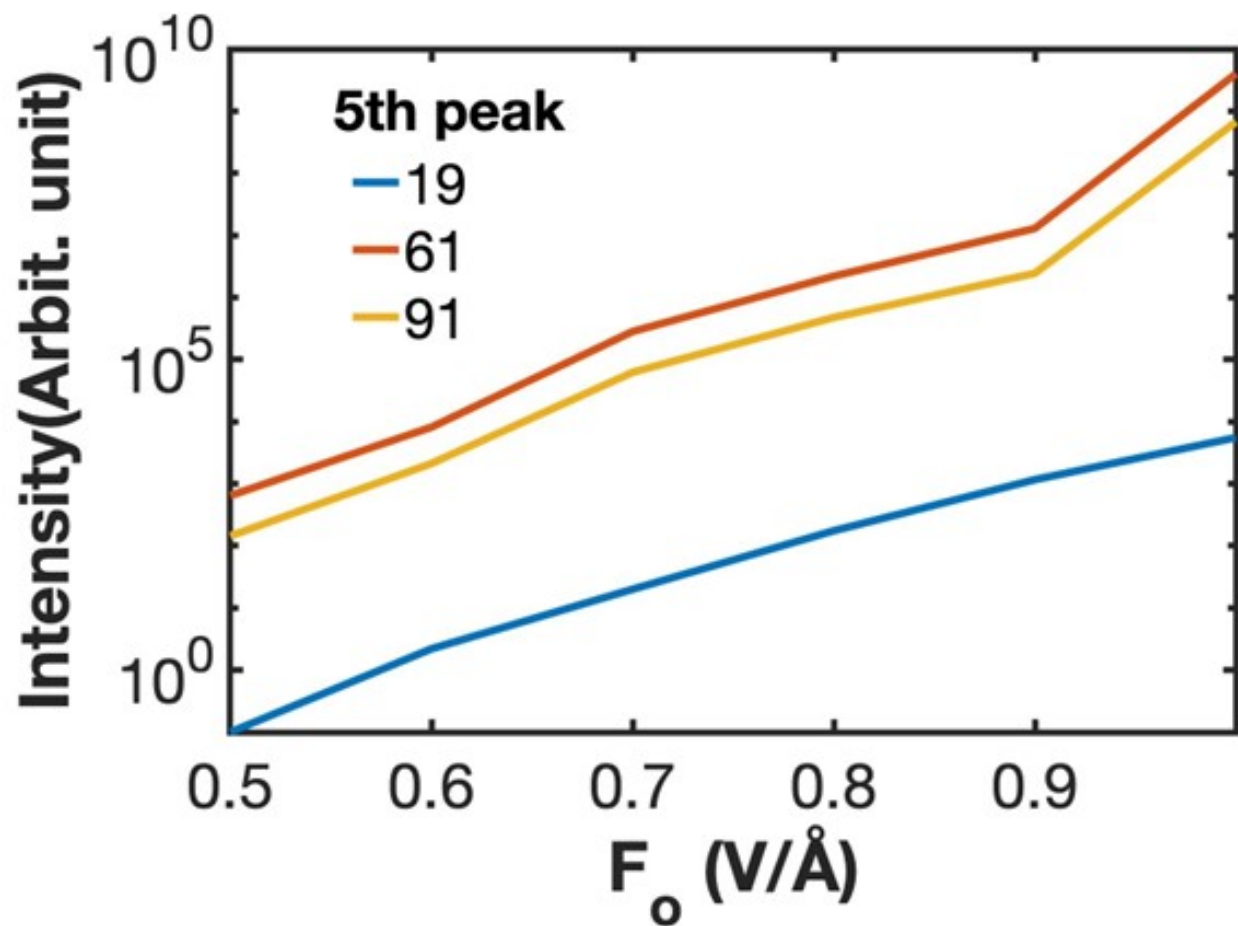


Figure 4.8 Intensity of the 5th harmonic versus the pulse field amplitude for different QD sizes. Here $\omega = 2.3$ rad/fs and $\tau = 3$ fs. The QD sizes, which are characterized in terms of the number of Mo atoms, are m

4.4 Conclusion:

When an optical pulse linearly polarized in the x-direction is applied to TMDC QDs, the nonlinear dipole moment, both in the x- and y-directions, is generated. Such nonlinear time-dependent dipole moment generates the radiation, the spectrum of which is characterized by the emission of high-order harmonics. The number of the generated high-order harmonics increases with increasing the field amplitude. The maximum number of high harmonics, that are generated, is realized at an intermediate QD size, corresponding to around 61 Mo atoms. These results suggest that as QD size increases, although the number of energy levels that are involved in the generation of radiation spectrum increases, the difference between the energy levels also decreases meaning that the QD spectrum becomes more continuous which suppresses the nonlinear effects. The maximum nonlinear response is realized at the QD size of 61 atoms when the later factor overcomes the effect of the first one.

CHAPTER 5

Summary:

We considered nonlinear response of TMDC quantum dots to an external ultrashort and strong optical pulse. The QDs were described within the three band tight-binding model assuming the coupling between d_{z^2} , d_{xy} , $d_{x^2-y^2}$ orbitals of Mo atoms only. MoS_2 QDs have in-gap edge states that are localized near the edges of the corresponding QDs. With increasing the QD size the band gap decreases asymptotically to 1.8 eV, which is the band gap of MoS_2 monolayers. Such behavior is consistent with experimental and other theoretical works and confirms the applicability of our model.

One of the effects of the edge states is an increase in the pulse absorption by TMDC QDs. At a low pulse amplitude, absorption is high and decreases sharply as amplitude increases and forms a plateau at a higher field amplitude. We calculated the absorption for QDs of different TMDC materials and observed that the absorption at low field amplitudes is inversely proportional to the band gap of the corresponding TMDC material.

When an optical pulse with polarization in the X-direction is applied we see a nonreversible dynamics, which is characterized by finite residual electron population of the excited QD states and a non-zero residual dipole moment, i.e., dipole moment after the pulse. The nonlinear electron dynamics in the field of the pulse also results in the generation of high harmonics, which were calculated for the pulse polarized along the x-direction. As field amplitude increases the number of generated high harmonics and their intensities increase. The cutoff frequency, i.e., the largest order harmonic that can be generated, also increases

as the field amplitude increases, which was observed for different pulse durations and QD sizes. Since for the TMDC monolayers the inversion symmetry is broken, the second-order harmonics can be generated, which is known as frequency doubling. The second harmonic generation can be used for the doubling of the laser frequencies.

The radiation spectra of TMDC QDs can be controlled by tuning the properties of in-gap edge states by introducing, for example, impurities and defects into TMDCs monolayer, which can be a future research direction. Also, the response of TMDC QDs should be sensitive to the polarization of an incident pulse. Thus, the intensity of high-order harmonics can be controlled by changing not only the pulse amplitude but also the pulse ellipticity. The corresponding high harmonics can also have ellipticity, which is different from the ellipticity of the incident pulse. The control of both ellipticity and the intensity of the generated high-order harmonics by changing the parameters, i.e., polarization and amplitude, of an incident pulse can be the direction of future research. It is also worth exploring the effect of the inter-layer coupling on both the absorption and the high harmonics generation by studying multi-layer TMDCs or arrays of quantum dots.

REFERENCES

- [1] A. Wirth, M. T. Hassan, I. Grguraš, J. Gagnon, A. Moulet, T. T. Luu, S. Pabst, R. Santra, Z. Alahmed, A. Azzeer, et al., Synthesized light transients, *Science* 334 (6053) (2011) 195–200.
- [2] O. Kfir, P. Grychtol, E. Turgut, R. Knut, D. Zusin, D. Popmintchev, T. Popmintchev, H. Nembach, J. M. Shaw, A. Fleischer, et al., Generation of bright phase-matched circularly-polarized extreme ultraviolet high harmonics, *Nature Photonics* 9 (2) (2015) 99–105.
- [3] P. Eckle, M. Smolarski, P. Schlup, J. Biegert, A. Staudte, M. Schöffler, H. G. Muller, R. Dörner, U. Keller, Attosecond angular streaking, *Nature Physics* 4 (7) (2008) 565–570.
- [4] S. Mao, F. Quéré, S. Guizard, X. Mao, R. Russo, G. Petite, P. Martin, Dynamics of femtosecond laser interactions with dielectrics, *Applied Physics A* 79 (2004) 1695–1709.
- [5] H. Fattahi, H. G. Barros, M. Gorjan, T. Nubbemeyer, B. Alsaif, C. Y. Teisset, M. Schultze, S. Prinz, M. Haefner, M. Ueffing, et al., Third-generation femtosecond technology, *Optica* 1 (1) (2014) 45–63.
- [6] A. Schiffrin, T. Paasch-Colberg, N. Karpowicz, V. Apalkov, D. Gerster, S. Mühlbrandt, M. Korbman, J. Reichert, M. Schultze, S. Holzner, et al., Optical-field-induced current in dielectrics, *Nature* 493 (7430) (2013) 70–74.
- [7] M. Schultze, E. M. Bothschafter, A. Sommer, S. Holzner, W. Schweinberger, M. Fiess,

- M. Hofstetter, R. Kienberger, V. Apalkov, V. S. Yakovlev, et al., Controlling dielectrics with the electric field of light, *Nature* 493 (7430) (2013) 75–78.
- [8] A. V. Mitrofanov, A. J. Verhoef, E. E. Serebryannikov, J. Lumeau, L. Glebov, A. M. Zheltikov, A. Baltuška, Optical detection of attosecond ionization induced by a few-cycle laser field in a transparent dielectric material, *Physical Review Letters* 106 (14) (2011) 147401.
- [9] E. Goulielmakis, V. S. Yakovlev, A. L. Cavalieri, M. Uiberacker, V. Pervak, A. Apolonski, R. Kienberger, U. Kleineberg, F. Krausz, Attosecond control and measurement: lightwave electronics, *Science* 317 (5839) (2007) 769–775.
- [10] P. Balling, J. Schou, Femtosecond-laser ablation dynamics of dielectrics: basics and applications for thin films, *Reports on progress in physics* 76 (3) (2013) 036502.
- [11] T. Otobe, M. Yamagiwa, J.-I. Iwata, K. Yabana, T. Nakatsukasa, G. Bertsch, First-principles electron dynamics simulation for optical breakdown of dielectrics under an intense laser field, *Physical Review B—Condensed Matter and Materials Physics* 77 (16) (2008) 165104.
- [12] V. Vénier, R. Taïeb, A. Maquet, Atomic clusters submitted to an intense short laser pulse: A density-functional approach, *Physical Review A* 65 (1) (2001) 013202.
- [13] K. Yabana, T. Sugiyama, Y. Shinohara, T. Otobe, G. Bertsch, Time-dependent density functional theory for strong electromagnetic fields in crystalline solids, *Physical Review B—Condensed Matter and Materials Physics* 85 (4) (2012) 045134.
- [14] P. J. Hasnip, K. Refson, M. I. Probert, J. R. Yates, S. J. Clark, C. J. Pickard, Density

- functional theory in the solid state, *Philosophical Transactions of the Royal Society A: Mathematical, Physical and Engineering Sciences* 372 (2011) (2014) 20130270.
- [15] B. Chimier, O. Utéza, N. Sanner, M. Sentis, T. Itina, P. Lassonde, F. Legaré, F. Vidal, J.-C. Kieffer, Damage and ablation thresholds of fused-silica in femtosecond regime, *Physical Review B—Condensed Matter and Materials Physics* 84 (9) (2011) 094104.
- [16] K. S. Novoselov, D. Jiang, F. Schedin, T. Booth, V. Khotkevich, S. Morozov, A. K. Geim, Two-dimensional atomic crystals, *Proceedings of the National Academy of Sciences* 102 (30) (2005) 10451–10453.
- [17] S. Z. Butler, S. M. Hollen, L. Cao, Y. Cui, J. A. Gupta, H. R. Gutiérrez, T. F. Heinz, S. S. Hong, J. Huang, A. F. Ismach, et al., Progress, challenges, and opportunities in two-dimensional materials beyond graphene, *ACS nano* 7 (4) (2013) 2898–2926.
- [18] M. Xu, T. Liang, M. Shi, H. Chen, Graphene-like two-dimensional materials, *Chemical reviews* 113 (5) (2013) 3766–3798.
- [19] B. Radisavljevic, A. Radenovic, J. Brivio, V. Giacometti, A. Kis, Single-layer mos₂ transistors, *Nature nanotechnology* 6 (3) (2011) 147–150.
- [20] K. F. Mak, C. Lee, J. Hone, J. Shan, T. F. Heinz, Atomically thin mos₂: a new direct-gap semiconductor, *Physical review letters* 105 (13) (2010) 136805.
- [21] H. J. Shin, S. C. Lim, J.-H. Son, et al., Ultrafast nonlinear travel of hot carriers driven by high-field terahertz pulse, *Journal of Physics B: Atomic, Molecular and Optical Physics* 51 (14) (2018) 144003.
- [22] Y. Y. Hui, X. Liu, W. Jie, N. Y. Chan, J. Hao, Y.-T. Hsu, L.-J. Li, W. Guo, S. P. Lau,

- Exceptional tunability of band energy in a compressively strained trilayer mos₂ sheet, ACS nano 7 (8) (2013) 7126–7131.
- [23] R. Ganatra, Q. Zhang, Few-layer mos₂: a promising layered semiconductor, ACS nano 8 (5) (2014) 4074–4099.
- [24] K. F. Mak, K. He, C. Lee, G. H. Lee, J. Hone, T. F. Heinz, J. Shan, Tightly bound trions in monolayer mos₂, Nature materials 12 (3) (2013) 207–211.
- [25] S. Mouri, Y. Miyauchi, K. Matsuda, Tunable photoluminescence of monolayer mos₂ via chemical doping, Nano letters 13 (12) (2013) 5944–5948.
- [26] J. R. Schaibley, H. Yu, G. Clark, P. Rivera, J. S. Ross, K. L. Seyler, W. Yao, X. Xu, Valleytronics in 2d materials, Nature Reviews Materials 1 (11) (2016) 1–15.
- [27] T. Cao, G. Wang, W. Han, H. Ye, C. Zhu, J. Shi, Q. Niu, P. Tan, E. Wang, B. Liu, et al., Valley-selective circular dichroism of monolayer molybdenum disulphide, Nature communications 3 (1) (2012) 887.
- [28] X. Xu, W. Yao, D. Xiao, T. F. Heinz, Spin and pseudospins in layered transition metal dichalcogenides, Nature Physics 10 (5) (2014) 343–350.
- [29] F. Bussolotti, H. Kawai, Z. E. Ooi, V. Chellappan, D. Thian, A. L. C. Pang, K. E. J. Goh, Roadmap on finding chiral valleys: screening 2d materials for valleytronics, Nano Futures 2 (3) (2018) 032001.
- [30] D. Xiao, G.-B. Liu, W. Feng, X. Xu, W. Yao, Coupled spin and valley physics in monolayers of mos₂ and other group-vi dichalcogenides, Phys. Rev. Lett. 108 (2012) 196802.

- [31] L. Xie, X. Cui, Manipulating spin-polarized photocurrents in 2d transition metal dichalcogenides, *Proceedings of the National Academy of Sciences* 113 (14) (2016) 3746–3750.
- [32] S. A. Vitale, D. Nezich, J. O. Varghese, P. Kim, N. Gedik, P. Jarillo-Herrero, D. Xiao, M. Rothschild, Valleytronics: opportunities, challenges, and paths forward, *Small* 14 (38) (2018) 1801483.
- [33] R. Bromley, R. B. Murray, A. D. Yoffe, The band structures of some transition metal dichalcogenides. iii. group vii: trigonal prism materials, *Journal of Physics C: Solid State Physics* 5 (7) (1972) 759.
- [34] L. F. Mattheiss, Band structures of transition-metal-dichalcogenide layer compounds, *Physical Review B* 8 (8) (1973) 3719.
- [35] Z. Y. Zhu, Y. C. Cheng, U. Schwingenschlögl, Giant spin-orbit-induced spin splitting in two-dimensional transition-metal dichalcogenide semiconductors, *Physical Review B—Condensed Matter and Materials Physics* 84 (15) (2011) 153402.
- [36] E. S. Kadantsev, P. Hawrylak, Electronic structure of a single mos2 monolayer, *Solid State Communications* 152 (10) (2012) 909–913.
- [37] S. Lebègue, O. Eriksson, Electronic structure of two-dimensional crystals from ab initio theory, *Phys. Rev. B* 79 (2009) 115409.
- [38] G.-B. Liu, W.-Y. Shan, Y. Yao, W. Yao, D. Xiao, Three-band tight-binding model for monolayers of group-vib transition metal dichalcogenides, *Physical Review B—Condensed Matter and Materials Physics* 88 (8) (2013) 085433.

- [39] B. Guo, Q.-l. Xiao, S.-h. Wang, H. Zhang, 2d layered materials: synthesis, nonlinear optical properties, and device applications, *Laser & Photonics Reviews* 13 (12) (2019) 1800327.
- [40] C. Lu, H. Xuan, Y. Zhou, X. Xu, Q. Zhao, J. Bai, Saturable and reverse saturable absorption in molybdenum disulfide dispersion and film by defect engineering, *Photonics Research* 8 (9) (2020) 1512–1521.
- [41] Y. Jiang, L. Miao, G. Jiang, Y. Chen, X. Qi, X.-f. Jiang, H. Zhang, S. Wen, Broadband and enhanced nonlinear optical response of mos₂/graphene nanocomposites for ultrafast photonics applications, *Scientific reports* 5 (1) (2015) 16372.
- [42] M. Liu, X.-W. Zheng, Y.-L. Qi, H. Liu, A.-P. Luo, Z.-C. Luo, W.-C. Xu, C.-J. Zhao, H. Zhang, Microfiber-based few-layer mos₂ saturable absorber for 2.5 ghz passively harmonic mode-locked fiber laser, *Optics Express* 22 (19) (2014) 22841–22846.
- [43] J. Pei, J. Yang, T. Yildirim, H. Zhang, Y. Lu, Many-body complexes in 2d semiconductors, *Advanced Materials* 31 (2) (2019) 1706945.
- [44] R. Ashoori, Electrons in artificial atoms, *Nature* 379 (6564) (1996) 413–419.
- [45] T. Chakraborty, *Quantum dots: A survey of the properties of artificial atoms* (1999).